JOURNAL OF GEOPHYSICAL RESEARCH, VOL. 101, NO. C12, PAGES 28,397–28,416, DECEMBER 15, 1996

Surface and radiative characteristics of the summer Arctic sea ice cover from multisensor satellite observations

Josefino C. Comiso

Laboratory for Hydrospheric Processes, NASA Goddard Space Flight Center, Greenbelt, Maryland

Ron Kwok

Jet Propulsion Laboratory, California Institute of Technology, Pasadena

Abstract. Accurate quantification and characterization of the Arctic summer ice cover are needed for mass balance, heat flux, and modeling studies in the region. A general assessment of the state and basic characteristics of the ice cover can best be done in summer because it is when the perennial component is fully revealed. The main source of summer ice information has been passive microwave and to a lesser degree active microwave data. However, the emissivity and backscatter of sea ice are abnormal and difficult to resolve during this time period, causing large uncertainties in the interpretation of satellite data. In this study we examined the state of the sea ice cover by using special scanning microwave imager (SSM/I), synthetic aperture radar (SAR), and advanced very high resolution radiometer (AVHRR) satellite data synergistically. The surface and radiative characteristics of the summer ice cover were evaluated in the context of three special events: onset of melt, melt ponding, and freeze-up. These events affect the emissivity and backscatter and may alter the albedo and ice structure. Onset of melt is readily detectable and is shown to migrate rapidly to the north in June. Melt ponding is not directly observable but is postulated to be the main cause of the decreases in brightness temperatures and large discrepancies between the SSM/I and SAR ice concentration results in many areas. In these areas, SAR and AVHRR results show concentrations near 100%, while the SSM/I data were as low as 70%. During freeze-up the ice signatures are still quite different from those of midwinter ice, but the ice concentrations from SSM/I generally agree well with those from SAR data. Our results show that, generally, the average ice concentration within the pack is usually greater than 90% during the summer, which is substantially larger than that inferred previously from passive microwave data. The use of combined SAR and SSM/I data may also provide melt-ponding fraction and first-order estimate of albedo in the Arctic region.

1. Introduction

A good characterization of the Arctic summer sea ice cover is essential to a complete understanding of processes in the region. Summer is the period when the true nature of the perennial sea ice cover is unmasked because at this time the surface is barren (almost no snow in most areas) and the interstitial ice that connects large floes during winter is either melted or broken up into small pieces. Because of high solar insolation during the summer and the strong contrast in the albedo of ice and open ocean, heat and radiative fluxes between the ocean and the atmosphere depend to a large degree on the extent and concentration of the ice cover. A study of summer ice is also a key to an accurate assessment of mass balance of the Arctic ice cover [*Comiso*, 1990; *Thomas and Rothrock*, 1993]. Together with observations of average thickness during the period, a quantification of actual summer ice cover provides a means to assess effects, if any, of a potential global warming due to increases in atmospheric CO_2 levels [*Manabe and Stouffer*, 1994]. Such assessment also enables the determination of meltwater production which largely influences the vertical stratification of the ocean and the biological productivity of the region.

The best available tool for studying the large-scale characteristics of the summer sea ice cover has been the passive microwave sensor [*Zwally and Gloersen*, 1977; *Carsey*, 1982; *Parkinson et al.*, 1987; *Comiso*, 1990; *Gloersen et al.*, 1992], the latest of which is the special scanning microwave imager (SSM/I) on board a satellite launched by the Defense Meteorological Satellite Program (DMSP). The sensor is noted for day/night, almost all weather capability and daily coverage of practically the entire Arctic region. However, interpretation of the summer brightness temperature data has been very difficult because of factors associated with above-freezing temperatures over ice during the period. The physical characteristics of the summer Arctic sea ice cover have been studied elsewhere [*Weeks and Ackley*, 1986; *Eicken et al.*, 1995]. Some factors such as surface melt, freeze/thaw cycle effects, melt-ponding effects, flooding, layering, and ice decay cause the emissivity of summer sea ice to be highly variable and sometimes unpredictable. The launch of the ERS 1 synthetic aperture radar (SAR) in July 1991 provided a good complement and possible alternative to the passive system. SAR is a day/night all weather sensor, as well, but it has a much better resolution (at 30 m) than that (>25 km) of the passive microwave sensor. While

Paper number 96JC02816.

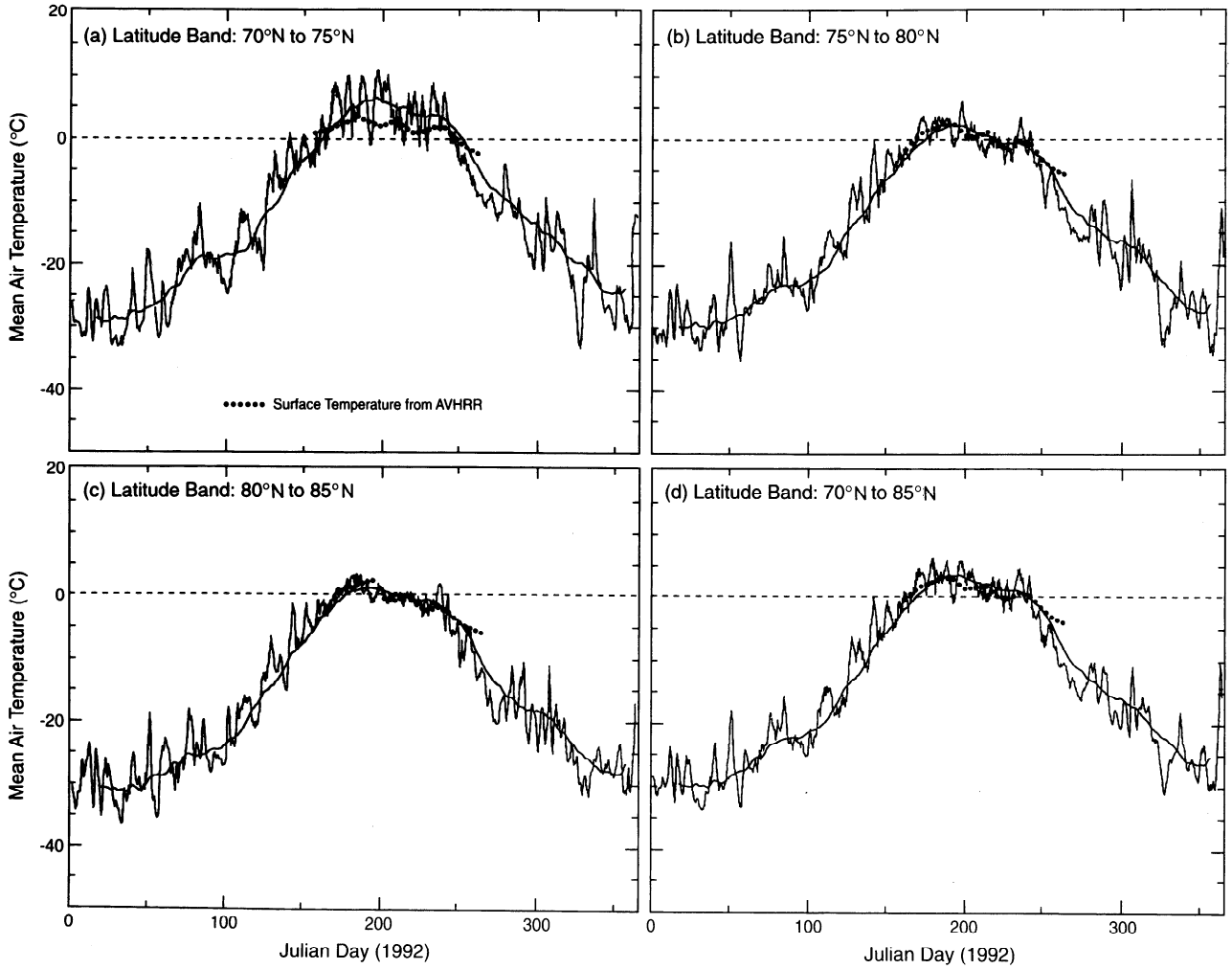

Figure 1. NMC surface air temperatures (12 hourly) from January 1 to December 31, 1992, averaged over (a) $70° > T_S > 75°$, (b) $75° > T_S > 80°$, (c) $80° > T_S > 85°$, and (d) $70° > T_S > 85°$ in the Beaufort Sea/Chukchi Sea region. Data points represented by small circles correspond to surface temperatures from AVHRR weekly maps. The smooth solid lines represent running weekly averages of the temperatures.

both systems are affected by similar surface problems during the summer [*Grenfell and Lohanick*, 1985; *Onstott et al.*, 1987; *Cavalieri et al.*, 1990; *Gogineni et al.*, 1992; *Beaven and Gogineni*, 1995], most ice floes and leads can be resolved with the SAR data and the dependence to a mixing formulation to derive ice concentration is not as critical as with passive microwave data. However, some ambiguities persist since sometimes open water within the ice pack is difficult to detect. Also, there are limitations in the use of ERS 1 SAR for large-scale/synoptic studies since the swath is only 100 km wide compared with 1390 km for SSM/I.

In this study we present results from an analysis of a time series of SAR and SSM/I data to identify summer events and infer the true character of the ice cover during this period. In particular, we looked at the behavior of the ice cover in general and examine detailed characteristics during onset of melt, freeze/thaw cycle, formation of slush and melt ponds, and refreezing. The time series data used for this study are mainly daily SSM/I data and orbital SAR data over Beaufort and Chukchi Seas in 1992. Advanced very high resolution radiometer (AVHRR) and meteorological wind and temperature data are also used to provide more accurate interpretation of environmental and surface effects. We take advantage of the high-resolution capability of the SAR system and the availability of meteorological data to identify areas of open water in the Arctic region for comparative analysis with passive microwave sensor data. The latter data set are then interpreted (together with AVHHR data) with a view of assessing potential problems of interpretation during the period caused by wetness and the presence of melt ponds and slush on the surface.

2. Satellite and Ancillary Observations

2.1. Meteorological Air Temperatures and Winds

Changes in surface properties during the summer are heavily influenced by surface air temperatures and wind. Surface air temperatures and pressure fields at 1000 mbar are routinely available from the National Meteorological Center (NMC) on a 12-hourly basis. Such temperatures provide a means for inferring surface characteristics and for analyzing brightness temperatures and backscatter in terms of surface conditions. Depending on value and persistence, above-freezing temperatures cause surface wetness, melt, formation of slush, and/or melt ponding. A time series of NMC air temperatures are

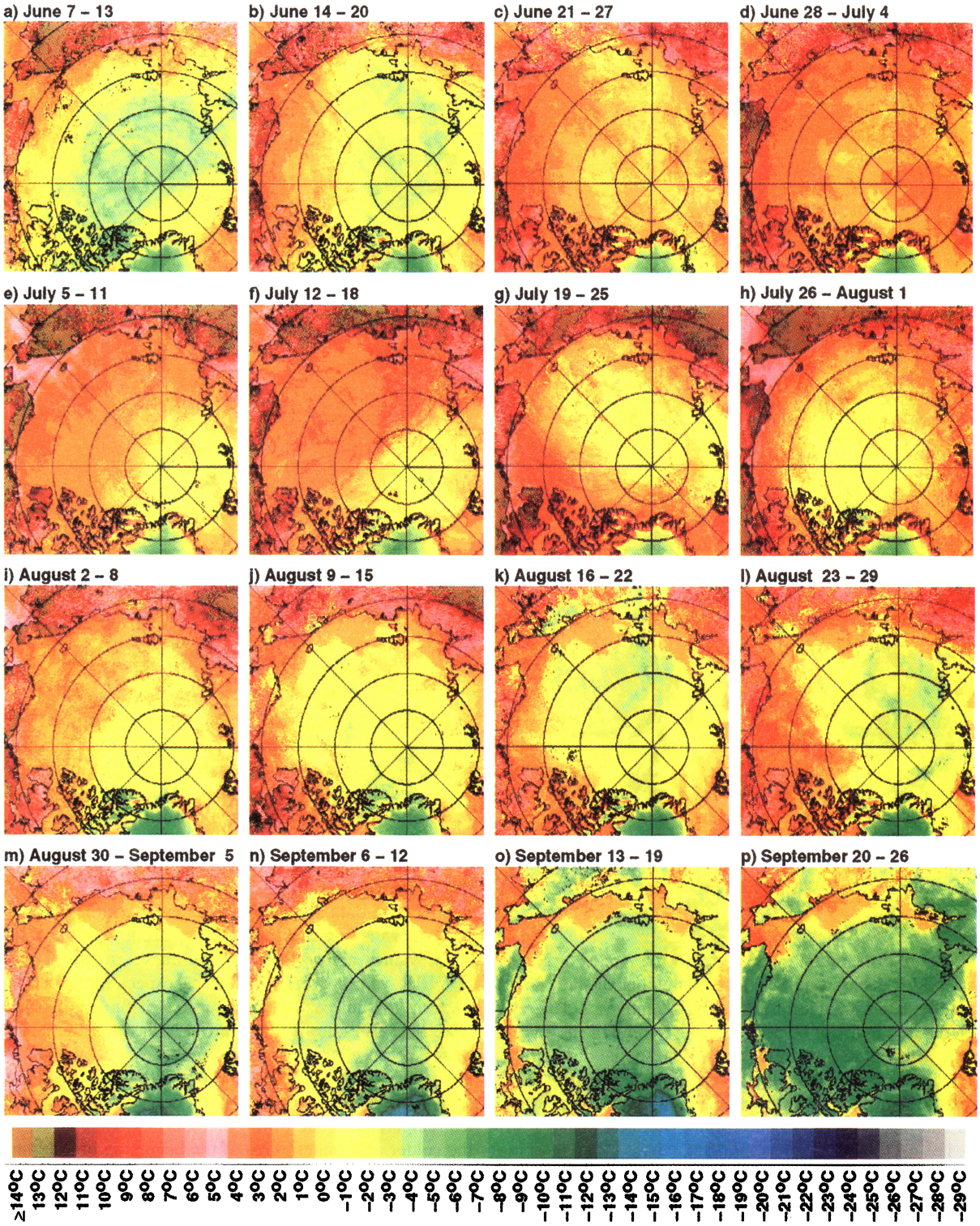

Plate 1. Color-coded weekly surface temperature maps using AVHRR global area coverage (GAC) data from the first week of June through the last week of September 1992.

presented in Figure 1 for various latitudinal zones in the Arctic: 70°N to 75°N (Figure 1a), 75°N to 80°N (Figure 1b), 80°N to 85°N (Figure 1c), and 70°N to 85°N (Figure 1d). The plots in Figure 1 indicate that the occurrence and duration of above-freezing temperatures are different in the different zones. Thus onset of melt varies from one region to another. In the southern region (70°N to 75°N), onset of melt may start as early as May 20, while in the northern regions (80°N to 85°N), it may occur about a month later. Generally, over the Arctic basin, the average air temperature goes above freezing at around the first week of June, while the freezing season starts in early September.

Examples of latitudinal changes in pressure fields, as derived from NMC data for different time periods, are shown in Figure 2a. Consistently high pressure values at all latitudes are appar-

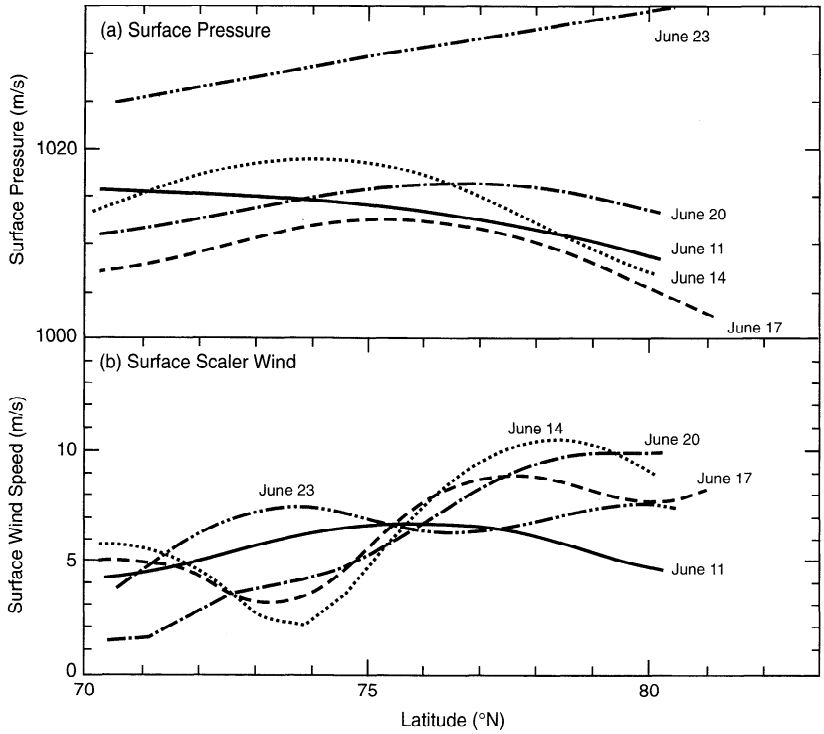

Figure 2. NMC 12-hourly data of (a) surface pressure and (b) scaler surface winds on June 11, 14, 17, 20, and 23.

ent on June 23 (day 175), while on other days the values appear considerably lower. The pressure fields are used to derive wind vectors such as those shown in Figure 2b. The wind speed was approximately uniform at around 75.5°N and 71.3°N with values at around 5 or 6 m/s, respectively, from June 11 through June 23. Daily fluctuations of 2 to 10 m/s occurred. These wind data were used, in combination with a model and temperature data, to discriminate open water from sea ice.

2.2. AVHRR Data

The spatial distribution of the fields in the Arctic, as generated by NMC, is based on only a small number of station and radiosonde data available for modeling and analysis. Thus the data generated may not be able to resolve some of the spatial features observed in the satellite data. The spatial distribution of temperature can be directly inferred from AVHRR thermal infrared radiances. The multichannel data have been calibrated and mapped in the same format (but at a higher resolution, i.e., 6.25 by 6.25 km) as the SSM/I data. Cloud masking was done using a technique that takes advantage of previous methods [e.g., *Massom and Comiso*, 1994; *Comiso*, 1994; *Key and Haefliger*, 1992; *Yamanouchi and Seko*, 1992]. The procedure does not overcome all the problems associated with discriminating clouds from snow surfaces. However, clouds move within hours, while snow and other surfaces are usually almost stationary during the same period. By taking difference maps between days and taking out areas where the difference is large, as done by *Comiso* [1994], the errors associated with clouds in the weekly averages are further minimized. A regression technique similar to that used in the open ocean [*McClain et al.*, 1985] was then applied using station and buoy surface air temperature data in the analysis. The precision in the retrieval of temperature from AVHRR data is estimated to be of the order of 1–3 K based on comparative analysis of results with buoy data and with station measurements at Prudhoe Bay and Point Barrow. The weekly images may have residual errors associated with imperfect cloud masking techniques. However, these and other IR sensor data provide the only means to assess large-scale spatial variations in surface temperatures. The AVHRR weekly data (indicated by small circles) are shown in Figure 1 to be in good agreement with the NMC temperature data at most latitudes except at the interval from 70°N to 75°N. At this interval (i.e., from 70°N to 75°N) the NMC values are several degrees above freezing, while the AVHRR values are restricted, as expected, to be close to freezing or subfreezing temperatures of the ice or snow surface. It is also known that there are biases in the NMC estimates because presently their model is not able to handle atmospheric inversions. Similarly, the differences in late September are likely because AVHRR detects the warmer surface ice temperature (due to thermal inertia), while NMC reflects the colder air temperatures at the beginning of autumn.

Color-coded maps of weekly averages of surface temperatures derived from AVHRR from early June through late September are presented in Plate 1. The series of images shows how the temperature isotherms varied during the 1992 summer period. During the first week of June a large part of the Arctic basin is still several degrees below freezing. It is also apparent that starting with the second week of June, the location of the ice edge is lost in the images because the ice surface temperature in the region is close to that of the adjacent open water. During the third week of June it is evident that the surface temperature in most areas of the Beaufort/Chukchi Seas region is already above freezing. The last week of June appears to be the warmest overall in this region, but for many areas the warmest week occurred in either July or August. The ice edge

location starts to reappear around the second week of August when start of freeze-up became apparent. A heat wave appeared in the last week of August, causing very warm temperatures in the Beaufort Sea region. However, by the second or third week of September it is apparent that freeze-up has occurred in the entire Arctic region.

2.3. ERS 1 SAR Data

The ERS 1 C band SAR ($\lambda = 5.6$ cm) transmits and receives radiation at vertical polarizations (VV) at a constant look angle of 20°. The SAR images used in this paper were downlinked to the Alaska SAR Facility where the data are calibrated and processed into image format. An image frame covers an area of approximately 100 km by 100 km on the Earth's surface. Although the original data have a resolution of 30 m by 30 m, the low-resolution versions which have pixel spacings of 100 m and footprints between 150 and 200 m were used for convenience in the analysis. At this pixel spacing, there are more than 40 looks per pixel and the variance in the pixel intensity due to speckle is minimized, making interpretation less ambiguous.

The normalized backscatter (σ) of each image pixel is computed using calibration coefficients provided with each product. The observed backscatter, based on product specifications, has absolute and relative calibration accuracies that are better than 2 and 1 dB, respectively [*Kwok and Cunningham*, 1994]. Absolute calibration accuracy measures our ability to observe the true normalized backscatter, whereas the relative calibration accuracy characterizes the stability of the system (i.e., ability to reproduce the same value when observing the same surface). We note here that the estimated noise equivalent of the radar is at approximately −24 dB (i.e., the noise level is equivalent to a radar target with this normalized backscatter). The backscatter of winter first-year and multiyear ice, the dominant ice types in the region, is above this level, having averages of −14 to −17 dB and −9 dB, respectively [*Kwok and Cunningham*, 1994].

During the cold winter period the backscatter of the most dominant types of sea ice surfaces in the Arctic (i.e., first-year, multiyear, and new ice) has been observed to be reasonably stable [*Onstott*, 1992]. Surface type is derived from SAR using a technique that makes use of a look-up table for the different polar surfaces including open water [*Kwok et al.*, 1992]. Ice concentration for a certain area is derived simply by calculating the fraction of the area covered by ice (regardless of ice type). During the summer the contrast in backscatter between different ice types is lost due to the presence of wet snow on the surface. But although the backscatter has changed to a value between that of multiyear ice and first-year ice, it is still possible to differentiate ice floes from open water if a combination of radiometric, geometric, and meteorological information is available. The backscatter of the summer ice cover is on the average −12 to −17 dB and seldom exceeds −10 dB. At C band VV the backscatter of open water is strongly dependent on the wind velocity. The ERS 1 scatterometer model function (CMOD3) provides a means for estimating the backscatter at 23° incidence angle for various wind speeds as a function of wind direction relative to the beam (Figure 3). For example, a wind speed of 6 m/s will cause a backscatter of about −6 dB (for wind direction of 70°, see arrow). The ice concentration is derived from SAR using the following procedure: (1) record the time and location of the image frame, (2) calculate the corresponding wind velocity and air temperature; (3) estimate from the CMOD3 function the expected backscatter of open water and use this value as the initial threshold, (4) visually adjust the threshold and the slope of the incidence angle dependence to identify all the leads with backscatter above this curve, and (5) calculate the ice concentration within each SSM/I pixel area over the entire image. The general assumptions are valid for most areas in the Arctic during summer. In practice, however, there is uncertainty in the wind velocity and the model function at the low incidence angle used here. Therefore we have to visually adjust the threshold to properly identify open water areas in a given image frame.

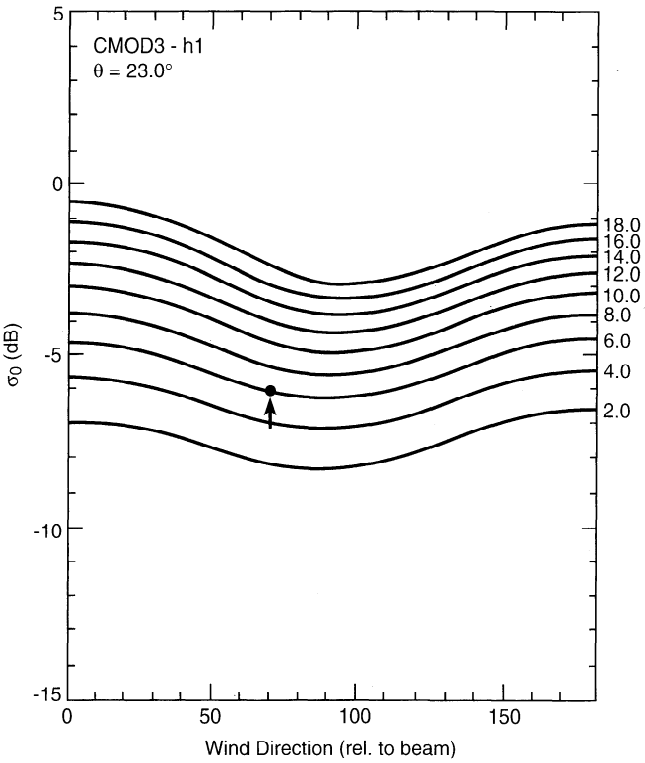

Figure 3. ERS 1 scatterometer model function (CMOD3) for converting backscatter into wind speed at 23° incidence angle. The numbers on the right correspond to wind speed in meters per second, while the arrow indicates that for wind direction of 70°, wind speed of 6 m/s will cause a backscatter of −6 dB.

2.4. Passive Microwave Data

Orbital brightness temperatures from all SSM/I channels were gridded to a standard rectangular polar stereographic map format [*Barry et al.*, 1993] for convenience in the analysis of the dual polarized multifrequency data. Daily averages were mapped to a 304 by 448 matrix with a grid size of 25 by 25 km, which is about the footprint size of the 37-GHz channel. The 19-GHz and 22-GHz channel data have coarser resolution but gridded the same way, while the 85-GHz channel data have better resolution also gridded the same way but at a finer matrix with a 12.5 by 12.5 km resolution. Of the seven channels, only four (19 GHz, 22 GHz, and 37 GHz at vertical polarization and 37 GHz at horizontal polarization) are used in this study.

Ice concentrations are derived using the bootstrap technique, as described by *Comiso* [1995], that takes advantage of

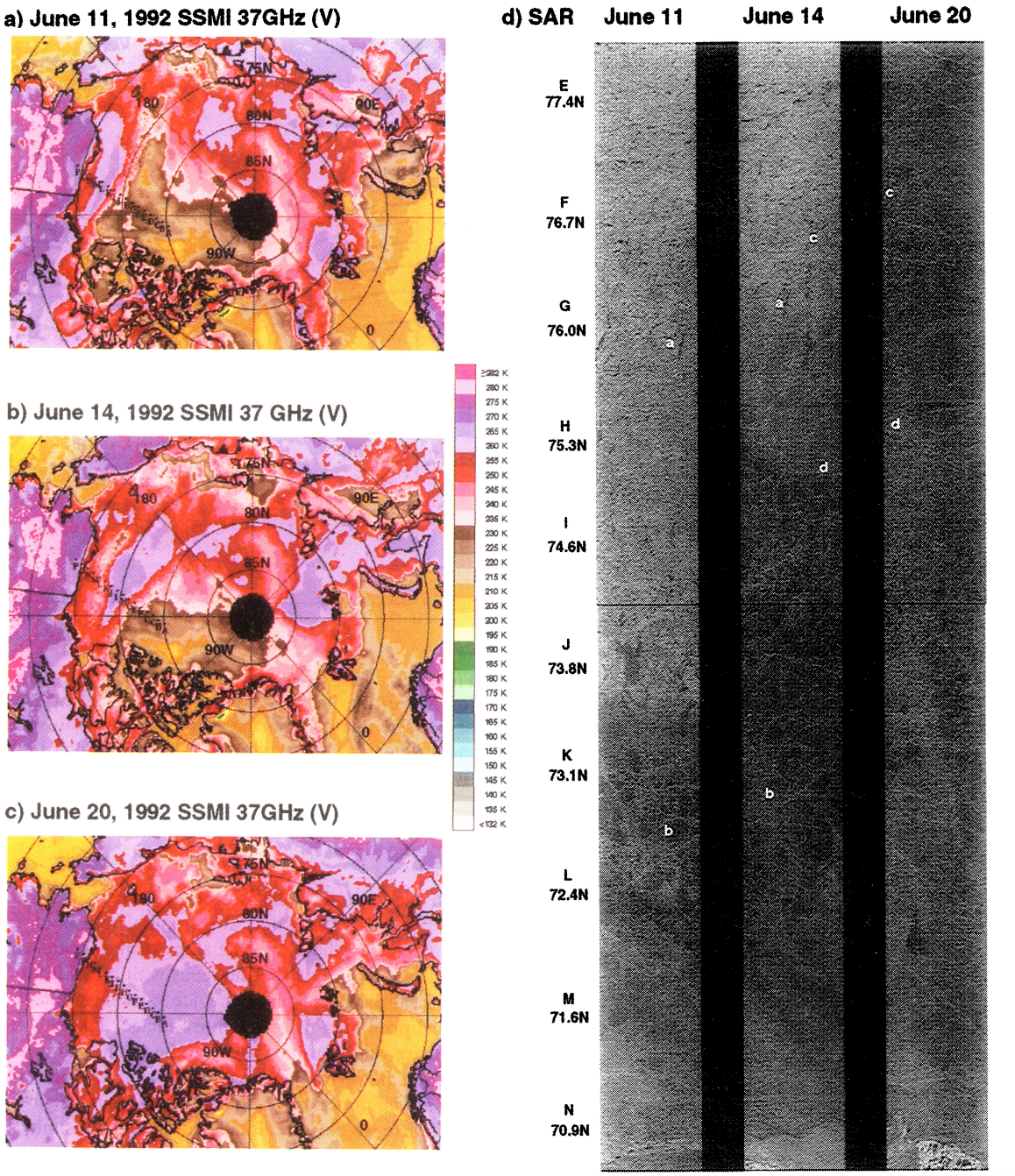

Plate 2. SSM/I brightness temperature maps at 37-GHz channel on (a) June 11, (b) June 14, and (c) June 20 and (d) SAR strip images in the Beaufort Sea on June 11, June 14, and June 20, 1992. The geographical locations of the SAR images are indicated by black dots labeled E, F, G, etc., in the SSM/I maps. (SAR images, Copyright ESA 1992)

unique multichannel distributions of the brightness temperatures of sea ice in highly compact regions. This algorithm utilizes two sets of channels: the HV37 set that uses the 37-GHz channels at vertical and horizontal polarizations and the V1937 set that uses the 19-GHz and 37-GHz channels at vertical polarization. The technique is most effective during the cold winter period when the passive microwave signature of sea ice is relatively stable. During this time the algorithm uses the HV37 set to obtain ice concentrations in much of the highly consolidated perennial and seasonal ice regions. The rest of the ice pack utilizes the V1937 set that is apparently less sensitive to effects due to ice layering, previously flooded surfaces, and the presence of new and young ice. The algorithm is designed for the most dominant ice types (first-year and multiyear ice) and may underestimate the concentrations in areas where there is a predominance of new ice as discussed by *Comiso et al.* [1992].

To calculate ice concentration from satellite data, it is not necessary to identify the ice type as done with other algorithms. The ice concentration C_I, corresponding to an observed brightness temperature T_B, is derived from a mixing formulation given by

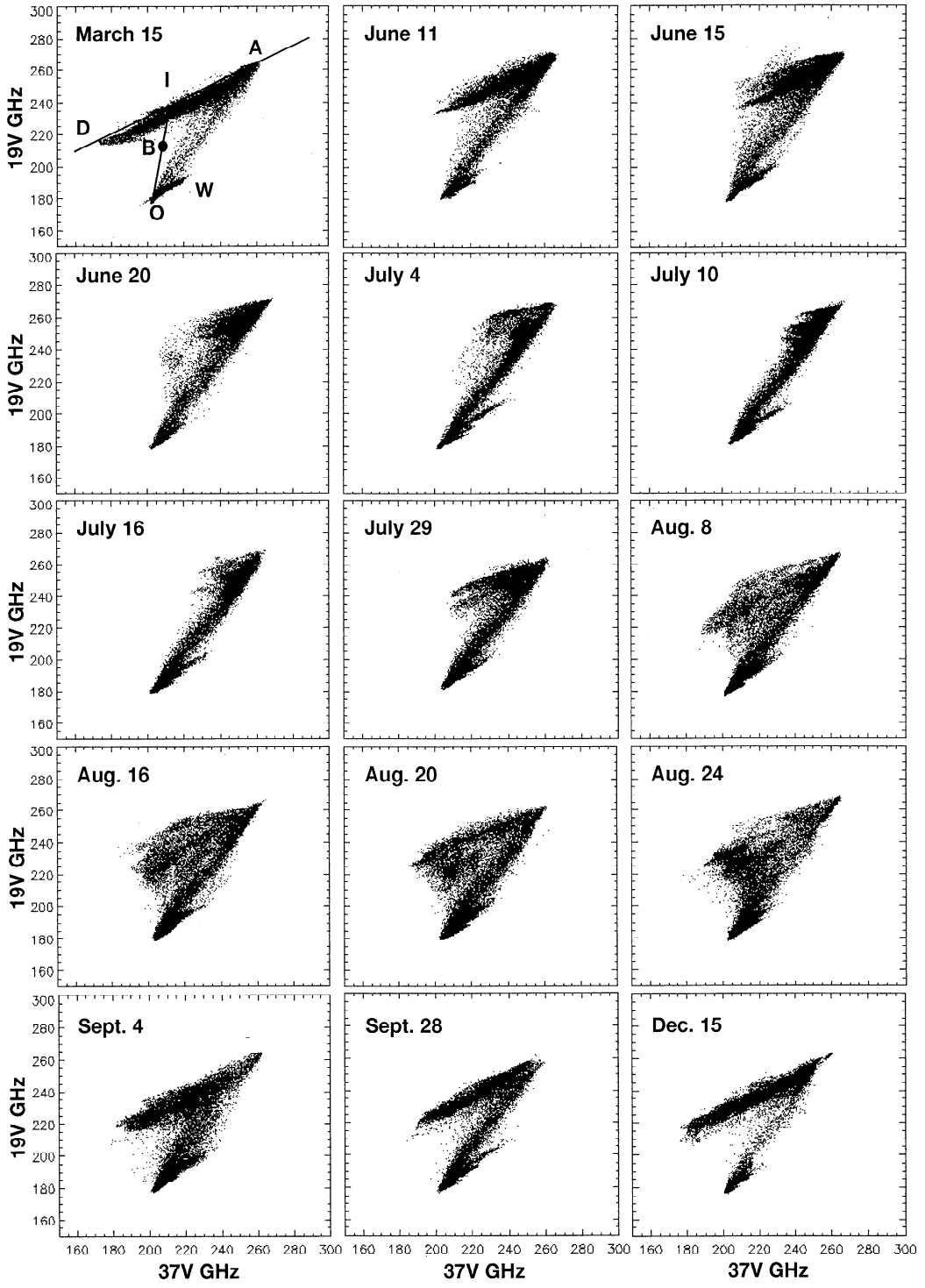

Figure 4. Scatterplot of 19V versus 37V for the period from March 15 through the summer and to December 15, 1992. The data points are from the Arctic region between 135°E and 225°E.

$$C_I = (T_B - T_O)/(T_I - T_O) \quad (1)$$

where T_O and T_I are reference brightness temperatures of open water and of consolidated ice, respectively. Equation (1) is valid, even for a one-channel system, as long as the appropriate reference brightness temperatures (i.e., T_O and T_I) are used for each data point. The reference brightness temperatures are inferred empirically using the HV37 and V1937 scatterplots and data from aircraft and in situ observations. In the summer, although the same sets of channels are used, some adjustments in the reference temperatures for 100% ice had to be made as will be discussed later.

3. Summer Events

During the summer period, large fluctuations in the emissivity [*Carsey*, 1985; *Comiso*, 1983; *Grenfell and Lohanick*,

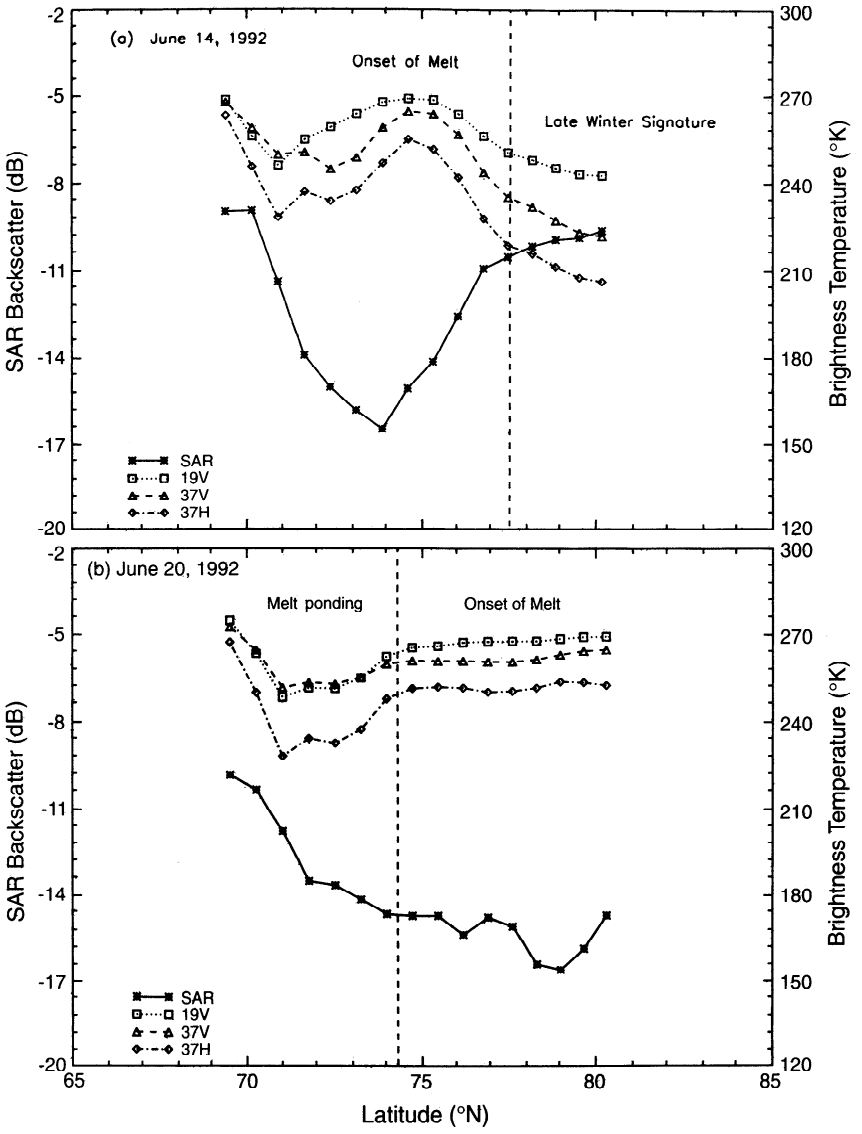

Figure 5. SSM/I brightness temperatures at 19 and 37 GHz and concurrent SAR backscatters during onset of melt on (a) June 14, 1992, and (b) June 20, 1992.

1985] and backscatter [*Onstott et al.*, 1987; *Gogoneni et al.*, 1992; *Winebrenner et al.*, 1994] of sea ice have been observed. These fluctuations are known to be highly correlated with the changing dielectric properties of the surface. The large variability of the emissivity is reflected in the series of 19-GHz versus 37-GHz scatter plots of vertically polarized brightness temperature data between 135°E and 225°E (Figure 4). The time series illustrates how the brightness temperature at each data point (representing approximately 625 km^2 in area) changes from mid winter (March 15), through the summer melt and melt-ponding period (June 11 to August 24), and on to the freeze-up period (August 8 to September 28). From winter through June 11, 1992, many of the data points representing near 100% ice in the central Arctic are confined within a narrow band between the labels A and B in the scatterplot. The wide range in the brightness temperature of ice reflects the varying effects of volume scattering from first-year ice with snow cover near A to low-salinity ice (i.e., multiyear ice) with snow cover near D.

Onset of melt apparently occurred from about June 15 through June 20, 1992, as indicated by changes in the clustering of data points along AD due to sensitivity of surface emissivity to the formation of moisture between the snow grains. During this period the surface become highly opaque and the brightness temperatures are less and less affected by volume scattering, causing the data points in Figure 4 to increase and migrate to the upper right (i.e., closer to point A). Subsequent formation of slush and melt ponding causes the data points to go down and cluster below point A. During freeze-up, data points move back toward point D as volume scattering effects get revived. Such phenomenon appeared to have occurred as early as July 29. Some data points with melt-ponded surfaces may lie below the consolidated ice cluster along AD until they are completely frozen. By December 15 the persistent winter signature has reappeared. The time sequence thus provides a means to understand how the signatures changes in response to changes in surface effects (e.g., wet snow to slush then melt ponds and eventually refrozen surface). The synergistic use of ancillary data including SAR data that provide accurate ice concentrations makes interpretation even less ambiguous. In

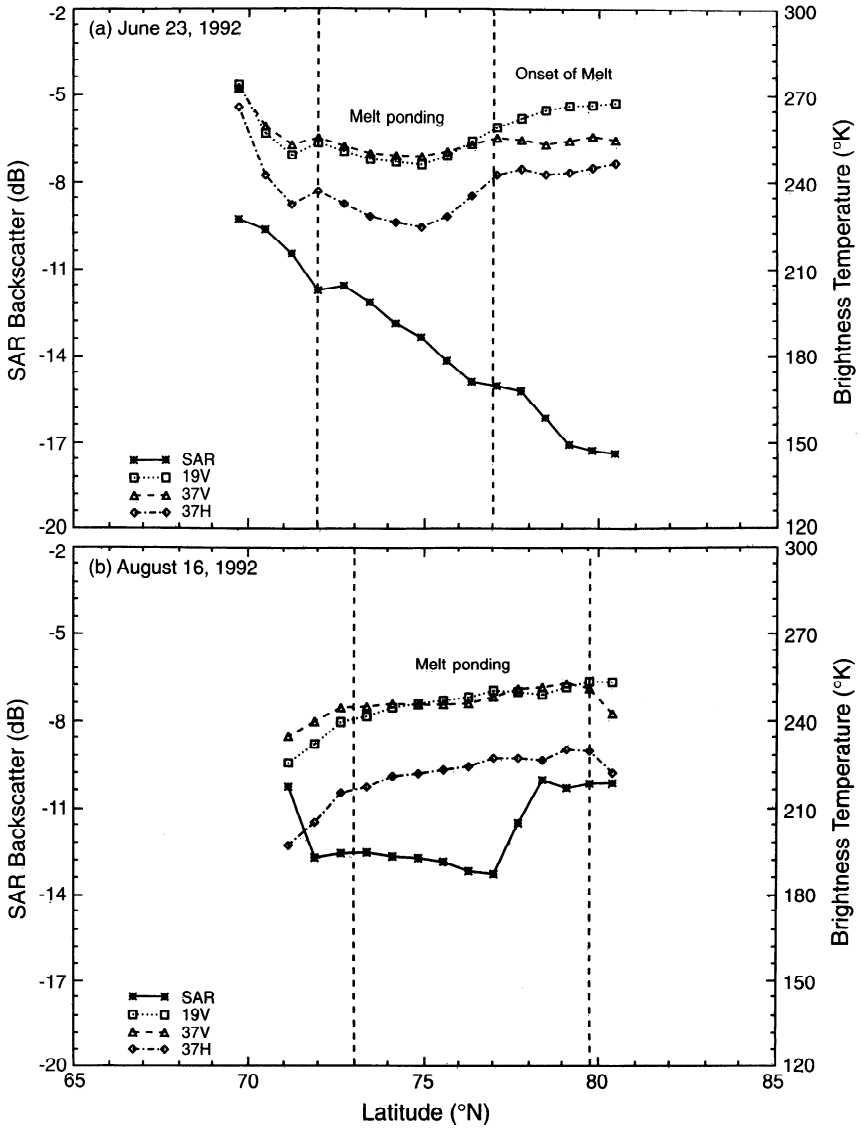

Figure 6. SSM/I brightness temperatures at 19 and 37 GHz and concurrent SAR backscatters during midsummer (meltponding) period on (a) June 23, 1992, and (b) August 16, 1992.

the following sections the occurrence of these events is discussed in the context of changes in the physical state and radiative properties of the ice cover.

3.1. Onset of Melt

The most remarkable change in the signature of sea ice occurs during onset of melt in late spring/summer period. By onset of melt we mean the event corresponding to the change in surface wetness over large areas as the average surface temperature in these areas exceeds freezing temperatures. This phenomenon is well illustrated by the sequence of SSM/I images at 37 GHz(V) starting with the image on June 11, when late winter signatures were still prevalent, through June 14, when onset of melt was apparent, to June 20, when onset of melt was dominant (Plates 2a–2c). The corresponding SAR images, the locations of which are indicated by labels E, F, G, etc., in the SSM/I images, show highly correlated changes in backscatter (Plate 2d). The SSM/I brightness temperatures and the SAR backscatter are evidently affected by the same surface phenomena at about the same time but in different ways. Slight wetness causes the imaginary part of the dielectric constant to increase about tenfold in both 19 and 37 GHz, making the absorption coefficient very high and therefore increasing the emissivity. At the same time the SAR backscatter decreases because the high absorption coefficient at the surface suppresses volume scattering contributions from below the surface.

Such effects are better quantified in coregistered SAR backscatters (in decibels) and brightness temperatures (at 19 V and 37 H and V), plotted in Figure 5. On June 14 the brightness temperatures are shown to be low in the southern region at around 71°N, where open water and/or flooding may be prevalent, and then go up to a maximum value at about 74°N, where onset of melt appears to be occurring, and go down to low values at high latitudes, where the surface is still cold and the multiyear ice signature is prevalent. The corresponding SAR backscatter shows similar response (in a reverse manner) with a minimum value of −17 dB at 74° reflecting onset of melt [*Winebrenner et al.*, 1994]. Such melt signals are apparent between 72°N and 74°N. On June 20 the brightness temperatures

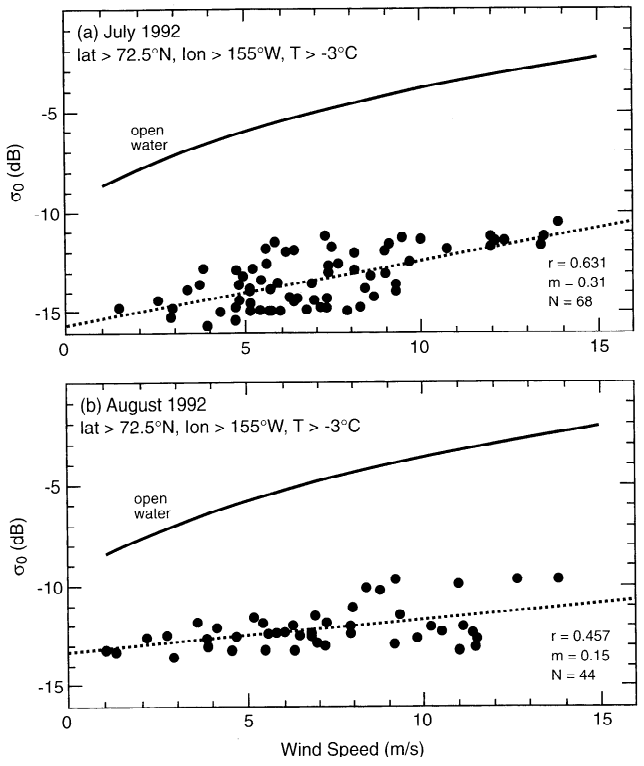

Figure 7. SAR backscatter as a function of wind speed for temperatures >-3°C during (a) July and (b) August.

between 74°N and 84°N went up to around 269 K for 19V, 263K for 37V, and 253K for 37H, reflecting near blackbody emissivities. Conversely, the backscatter of sea ice in the same region went down to as low as −16.8 dB at 79°N. The combined SAR and SSM/I data thus provide an almost unambiguous signal of onset of melt, especially if previous conditions of the surface are known.

3.2. Melt Ponding

Melt ponds are formed as the surface air temperatures become persistently above freezing. It has been reported that in some places in the Arctic during the summer, as much as 30% of the surface is covered by melt ponds (e.g., H. Eicken, private communication, 1991; W. Tucker, private communication, 1994). Since water is opaque to microwave radiation, melt-ponded areas have signatures identical to those of open water in leads or between ice floes. However, since only a fraction of the 25 by 25 km area observed by the passive microwave sensor is melt ponded, the actual brightness temperature is somewhere between that of open water and ice. Passive microwave data alone cannot be used effectively to discriminate melt-ponded areas because the signature is practically identical to that of mixtures of open water and ice. SAR data are also difficult to use to discriminate melt-ponded areas because the latter features are normally smaller than the size of the footprint. However, the SAR algorithm usually classifies melt-ponded ice floes as 100% ice. In this context the two sensors can be used in concert to detect occurrences of melt ponding.

Depending on fractional extent, melt ponding causes a general decrease in the effective emissivity of sea ice. Since the contrast between ice and water is higher at lower than higher frequencies, the magnitude of the decrease in brightness temperatures due to melt ponding is greater at lower than higher frequencies. The transition from onset of melt to melt ponding appears to be evident already in the case shown in Figure 5b at the latitude location between 71°N and 74°N. In this area the brightness temperatures went down significantly with the frequency dependence manifested by lower values at 19 GHz(V) than at 37 GHz(V), while at >75°N the reverse is true. The same phenomenon is evident on June 23, as shown in Figure 6a, with the effects propagated at higher latitudes. At latitudes >75°N the brightness temperatures at all channels have relatively higher values, indicating that onset of melt was still going on.

To discuss this phenomenon in a more general context, we point out that on June 23, the prevalent surface temperatures inferred from AVHRR images (Plate 1) and NMC temperatures (Figure 1) are near or above freezing. The series of SAR images in Plate 2 shows the latitudinal progression of the melt event. In the SAR images, divergence is not apparent, indicating that there was no drastic change in the ice concentration during the period. On the other hand, the SSM/I brightness temperatures over the same region are substantially lower than those at higher latitudes, despite higher physical temperatures of the surface. If ice concentration did not change, as indicated by SAR data, the decrease in brightness temperature must be due to melt ponding. It would have been about 12 days since onset of melt, and by June 23 the surface may have evolved into either slush or melt-ponded surface. This is possible, since for an average snow thickness of about 20 cm, a few days of above freezing temperatures can melt the snow completely, assuming that the subsurface temperature of the snow is not too cold.

The same phenomenon can be inferred from the data in various places throughout the summer. An example of a late season occurrence in the inner pack is shown in Figure 6b using data on August 16. The areas where melt ponding appears to have occurred are where the brightness temperatures at 19 and 37 GHz are comparable (or with the 19V values slightly lower than those of the 37V). This is substantially different from melt onset conditions when both channels are well separated and their highest values are about 269 K and 263 K for 19 GHz(V) and 37 GHz(V), respectively. These relative values may, however, change on account of changing conditions (e.g., wet to dry) of the ice surfaces surrounding the melt ponds.

As indicated earlier, the SAR backscatter tends to increase slightly a few days after onset of melt. The increase may be due partly to melt-ponding effects since in the presence of strong enough wind, surface waves over melt ponds could lead to higher backscatter. To investigate this effect, we plotted in Figure 7 the SAR backscatter as a function of wind speed for both July and August data in areas where the surface air temperatures are higher than −3°C and the ice concentration is near 100%. It is apparent that the variance in backscatter is greater in July than in August and the mean values are generally higher in August than in July. This suggests higher melt-ponding fraction in August than in July. The plots in Figure 7 show slight trends with slopes of 0.31 and 0.15 and correlation coefficients of 0.63 and 0.46, respectively, for July and August. It should be noted that at wind speeds above 11 m/s, the backscatter was basically constant. This may be partly because the melt ponds are usually shallow and the maximum effect of wind on the backscatter occurs at an intermediate wind velocity. The relatively weak correlation and large scatter of data points may also be caused by other factors such as the presence of ridges in the region.

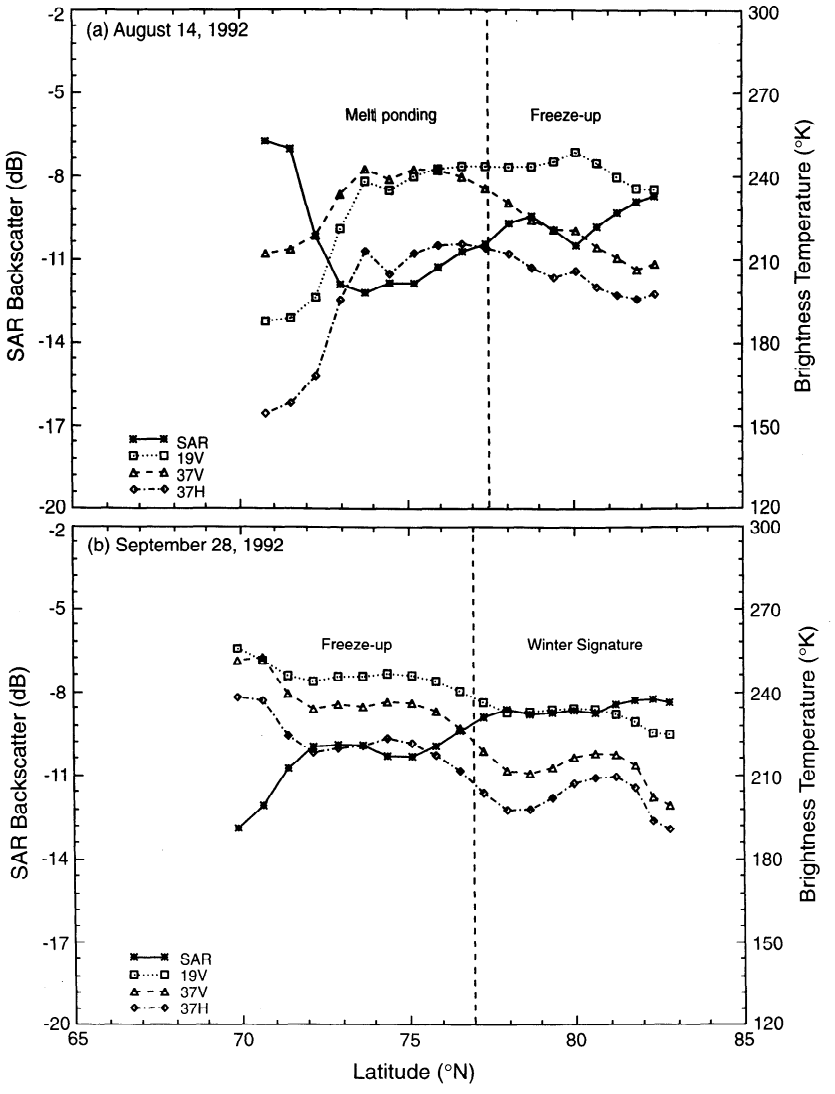

Figure 8. SSM/I brightness temperatures at 19 and 37 GHz and concurrent SAR backscatters during autumn conditions on (a) August 14, 1992, and (b) September 28, 1992.

3.3. Summer/Autumn Transition

The signature of sea ice changes considerably from summer to autumn. During late summer the surfaces become basically barren and deprived of snow cover in most places. The presence of chunks of slush in most surfaces has also been observed (H. Eicken, private communication, 1992). Autumn signatures are strongly influenced by freeze-up and subsurface cooling. The set of scatterplots in Figure 4 shows the reappearance of a multiyear ice signature as early as August 8. In subsequent days the plots show the unfolding of the effects of having different types of surfaces (i.e., a combination of dry multiyear ice surface, melt ponds, partly frozen melt ponds, and completely frozen melt ponds) in an SSM/I pixel.

The appearance of an early autumn signature at high latitudes is suggested in the set of plots for August 14 as shown in Figure 8a. At 80°N the 19-GHz brightness temperature reached a peak value of around 250 K and started to go down slightly at higher latitudes, while the 37 GHz data show a sharper decrease in brightness temperature. These decreases in brightness temperatures occur concurrently with increases in SAR backscatter, indicating that volume scattering of the radiation in the ice is already occurring. Peak value is also observed at lower latitudes at 37 GHz, which is more sensitive to the upper layer than the 19 GHz because of shorter wavelength. This suggests that the top portion of the ice is already cold and dry in this region at this time.

By late September the surface of the entire Arctic region is expected to be refrozen (see Figure 1). Typical signatures at this time are shown in Figure 8b. The plots show that from high values at around 70°N, the brightness temperatures at all channels basically go down with latitude with the exception of slight increases near 80°N. Concurrently, the corresponding SAR backscatter shows similar but opposite trend effects. The spatial changes in signature are associated with three radiometrically different areas, namely (1) a high emissivity (or low backscatter) area at 70°N, (2) an intermediate area between 71°N and 75°N, and (3) a low-emissivity (high backscatter) area at >76°N. These regions correspond to the first-year ice, transitional ice, and multiyear ice areas, respectively and the signatures are consistent with those expected of dry and cold ice surfaces [*Eppler et al.*, 1992; *Onstott*, 1992]. The transitional ice may include second-year ice cover which has been observed to

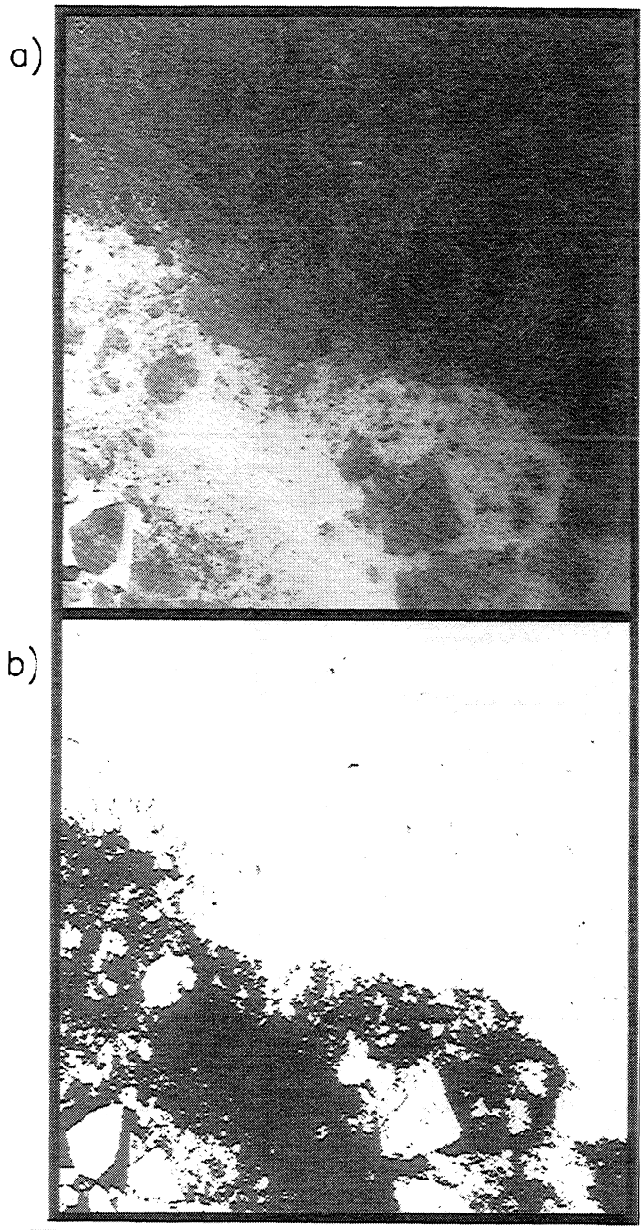

Figure 9. (a) SAR image before the analysis and (b) binary SAR image after the analysis with white representing ice cover (air temperature = 1.8°C and wind speed = 15 m/s). (SAR image, Copyright ESA 1992)

have intermediate emissivities [*Eppler et al.*, 1992]. In midwinter the contrast in emissivity and backscatter between ice types in these regions becomes greater because of enhanced volume scattering effects.

During autumn the large scatter of data points for consolidated ice in the V1937 and HV37 sets observed for the summer is minimized because the surfaces in most areas are consistently dry. Although the signatures are not quite the winter values yet, the data points are mainly in the proximity of the line AD that is used to obtain the reference temperature for 100% ice by the bootstrap algorithm. Thus at this time the uncertainty in the ice concentration determination approaches that of winter values.

4. Observed Characteristics of the Summer Ice Cover

4.1. Ice Concentrations From SAR Data

The technique described previously for the discrimination of ice from water in the summer SAR images was generally effective. An example for a case where the discrimination is usually difficult but the air temperature is 1.8°C and the wind speed is 15 m/s is shown in Figure 9. The calibrated SAR image is shown in Figure 9a, while the inferred binary surface classification that provides ice concentration is shown in Figure 9b. A minimum wind speed of approximately 4 m/s is needed to insure that open water has a backscatter which is reasonably distinct from that of other surfaces. During calm conditions, ice concentrations are also derived, but the uncertainties are larger because open water in the pack would have backscatters similar to those of new, young, or wet ice.

Among other sources of errors are those due to wind fetch, melt ponding, and the finite resolution of the sensor. For a given wind forcing the capillary waves grow exponentially to its limiting value (i.e., wavelengths in the range of 0.7–7.0 cm) in a matter of seconds [*Donelan and Pierson*, 1987], long before the fetch limit is reached. Ambiguities in the identification of open water due to wind shadow effects caused by rafting and/or ridging at the ice water boundaries are expected. However, the net effect on the calculation of ice concentration for such cases has been estimated to be small in the summer because of low backscatter due to surface wetness.

The resolution of the SAR data used in this study is such that most melt ponds are not resolved. The SAR algorithm identifies melt-ponded ice floes as ice. Hence, if we assume open water as existing only in leads and between identifiable floes, the presence of melt ponds would cause minimal errors in the retrieval of ice concentration. Indeed, the backscatter from surfaces identified as those of ice in midsummer and when the surface air temperature is >3°C was found to be distinct from those of open water.

The presence of small leads not resolved by SAR can cause overestimates in the derived ice concentration. Good statistical measurements of lead widths and areal fraction of unresolved leads during the period would be useful to assess this effect. However, such data do not exist in the literature. An analysis of a Landsat image during spring by R. W. Lindsay (personal communication, 1994) in the Beaufort Sea indicated that the percentage ratio of the area covered by leads with widths less than 100 m to the total lead area is approximately 22%. Within that image the mean lead width is 140 m with very few leads more than 500 m wide. In midsummer the ratio of unresolved leads is likely higher, but assuming that the aforementioned lead statistics can be considered typical for the entire Arctic region, the SAR resolution problem would cause a 2% error ($=0.22 \times 10\%$) in regions of 90% ice cover. Thus the actual ice concentration in areas where the SAR ice concentration quoted in this study is 100% is expected to be less than 98%. More measurements on lead statistics are obviously required to better establish the absolute values and errors.

4.2. Ice Concentrations From SSM/I Data

In Figure 4 the V1937 scatterplot on March 15 shows typical winter distribution. The data points along the line AD represent the inner pack of Arctic region where the ice concentration is close to 100% in most areas. The data points along AD are used in conjunction with aircraft and in situ data as the

Table 1. Slopes and Offsets Used by the Bootstrap Algorithm for SSM/I Data in the Arctic During Winter and Summer

	Months	Slope β	Offset α	M_0
100% ice for winter (cold) conditions				
(37H versus 37V)	October–June	1.000	−12.0	
(19V versus 37V)	October–May	0.553	117.0	
100% ice for summer (warm) conditions				
(37H versus 37V)*	July 1–18	1.226	−70.0	
	July 19–Aug. 4	1.033	−25.0	
	Aug. 5–Sept. 28	0.993	−14.0	
(19V versus 37V)	June–September	0.560	119.0	
Open ocean masking for winter (cold) conditions				
(19V versus 22V)	October–May	0.567	78.0	
(22V–19V)				>14 K
Open ocean masking for summer (warm) conditions				
(19V versus 22V)	June–October	0.580	72.26	
(22V–19V)				>23 K
Open water tie points for cold conditions				
19V = 176 K, 37V = 200 K, 37H = 127 K				
19V = 176 K, 37V = 200 K				
Open water tie points for summer conditions				
19V = 178 K, 37V = 201 K, 37H = 128 K				

*The slopes and offsets were further refined on a day-to-day basis using an automated system.

basis for inferring the 100% ice line which serves as the reference brightness temperature (i.e., where T_I is located) for ice. Also, data points along the line OW are from ice free ocean, with those near O and W affected least or most, respectively, by adverse weather conditions and waves. Since open water in the inner pack is least affected by waves and storms, the reference brightness temperature for open water, T_O, is taken as a point close to the minimum value at O. For each data point in the scatter plot (e.g., at location B, which has been enhanced for illustrative purposes), ice concentration is calculated from the ratio of the magnitude of the lines OB to OI, where I is the intercept of OB and AD. This ratio is equivalent to the ratio in (1) and is used instead of the latter because it avoids the singularity when $T_I = T_O$, as described by *Comiso* [1986; 1995]. The HV37 set is used, instead of the V1937 set, in more predictable highly consolidated ice areas, such as those in the Arctic region during winter, because it better accounts for spatial changes in surface temperature and provides better resolution. The algorithm also utilizes the 22-GHz channel at vertical polarization for masking the open ocean region as discussed by *Comiso* [1995].

Previous studies by *Emery et al.* [1994] indicated that the bootstrap SSM/I algorithm, which was optimized for winter conditions, provided lower ice concentrations than those derived from AVHRR during the summer period. The SSM/I results for 1992 were found to be considerably lower than the SAR results as well. In this study the reference temperatures were refined, as indicated in Table 1, to better adjust to the changing emissivity of sea ice during the summer. The results provided better agreement with the SAR data, but the discrepancies are still large in many areas.

A series of color-coded ice concentration maps derived from the SSM/I data are shown in Plate 3. The black dots (labeled A, B, C, ···, etc.) correspond to the locations of the SAR images used in this study. The series of maps shows the evolution of the Arctic ice cover from onset of melt to the freeze-up period. The Arctic region is shown to be still almost fully covered by sea ice on June 11, 1992. During this time, some small areas with ice concentrations between 70 and 90% are evident in Fram Strait, Chukchi Sea, Beaufort Sea, Laptev Sea, and Barents Sea. The sizes of these relatively lower ice concentrations areas increased considerably during the next several days. Large areas in which the concentrations are between 70 and 90% are evident in the inner ice region of the Chukchi Sea (175°E, 76°N). Unfortunately, we do not have SAR data for those regions and could not say definitely if melt ponding was going on. However, on August 8, August 16, and August 24, similar effects are observed in the western part of the Beaufort Sea (185°E, 73°N), and in these case, there was coincident SAR data. In these cases the SAR ice concentrations were mostly close to 98%, indicating that melt ponds were likely present in the area. By September 28 the SSM/I ice concentrations are shown to be close to 100% in the inner regions.

4.3. Comparative Analysis

Because of the narrow swath width of the SAR data (100 km compared with 1390 km for SSM/I) and limited data coverage for the Arctic, the observational area covered by SAR is much more limited than that by SSM/I. Our study is focused on SAR data acquisitions along approximately two transects: one along the Beaufort Sea and the other along the Chukchi Sea. The locations of the SAR images for the days shown in Plate 2 and the approximate orientation of the orbits are indicated by black dots, which are the centers of each image.

Although the SAR backscatter is also sensitive to changes in surface dielectric properties in summer, its high resolution enables identification of distinct features (e.g., see floes identified as a, b, and c in the SAR images in Plate 2d) as the backscatter changes with time. Identification and analysis of such features provide a means to evaluate whether the changes in backscatter are associated with surface changes only or with actual decay of ice floes or widening of leads. The images show that in most cases, edges of ice floes are identifiable and linear features that correspond to leads and ridges can be recognized by visual inspection. The backscatter is shown to change from one day to the next, but the same ice features remain basically unchanged in size and shape, indicating that divergence and decay were minimal and that the ice concentration did not change much. Additional SAR images, in strip format, taken during other time periods of summer are shown in Figure 10.

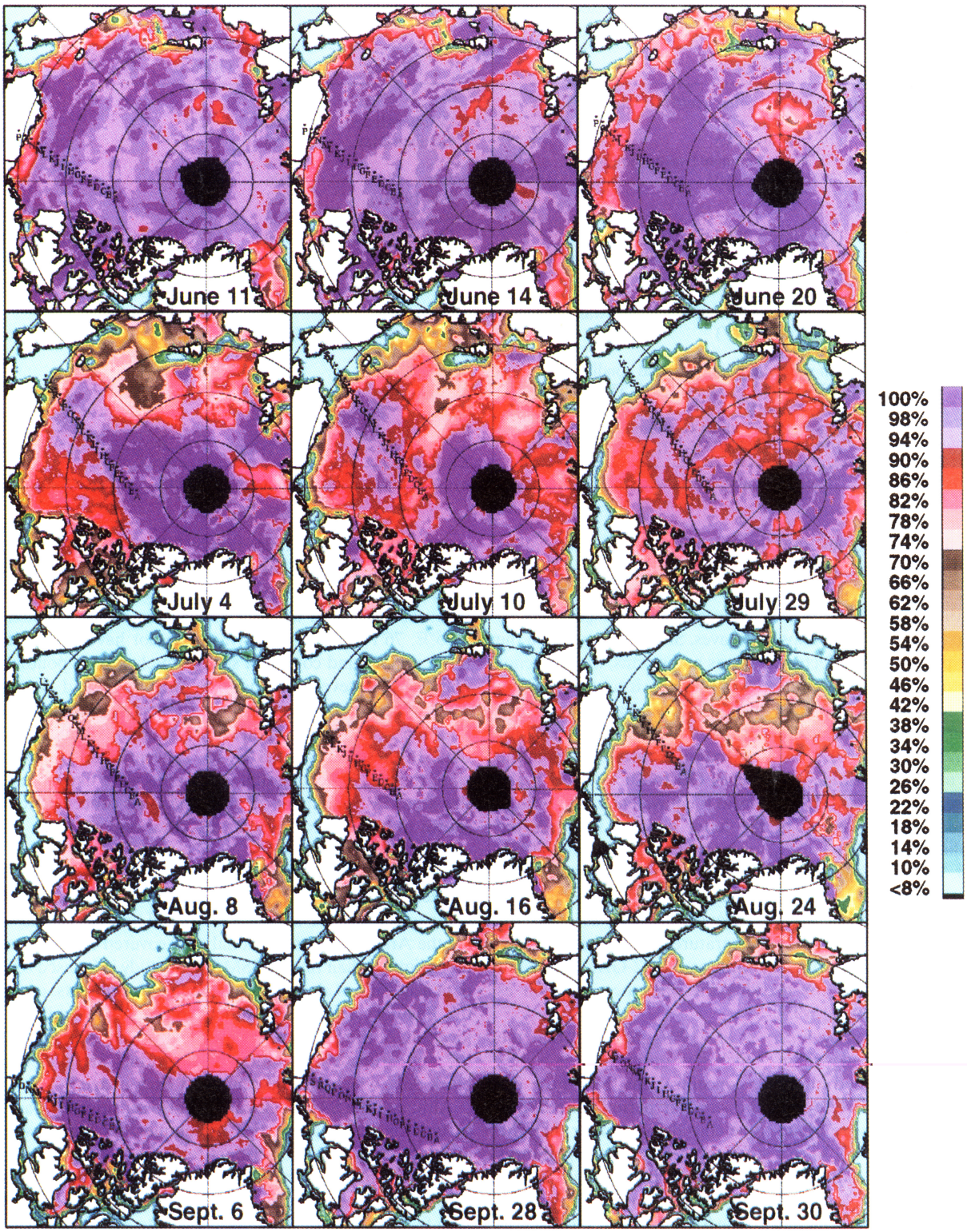

Plate 3. Color-coded ice concentration maps from SSM/I brightness temperature data using the bootstrap algorithm for the period from June through September. Black dots labeled A, B, C, etc., are locations of coincident SAR images used in this study.

As in Plate 2 the orientation of the strip images is such that the top part corresponds to areas near 78°N, while the lower part is at about 71°N. Again, highly compact ice cover is apparent in these images. Wind data were used to remove some of the ambiguities in discriminating open water, as discussed earlier, and whenever possible, relevant information available from the time series of images was utilized in the interpretation.

Quantitative comparisons of ice concentrations derived from SAR and SSM/I data along the study transects during different time periods in summer are shown in Figure 11. Each

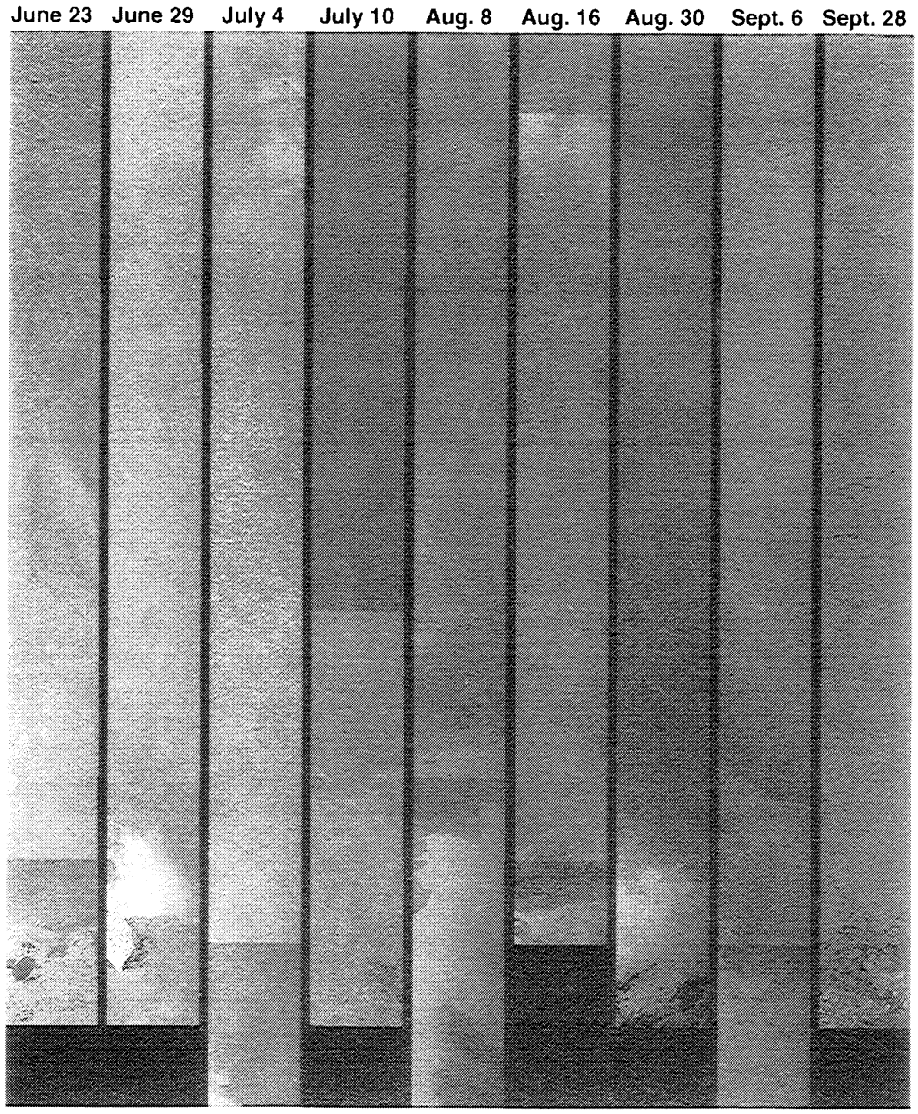

Figure 10. SAR strip images along the study transects on June 23, June 29, July 4, July 10, August 8, August 16, August 30, September 6, and September 28, 1992. Upper part is near 78°N, while the lower part is about 71°N. (SAR images, Copyright ESA 1992)

data point in the SAR plots represents the average concentration derived from the 185 km by 185 km SAR images, while that in the SSM/I plot represents the corresponding average concentration over the same area. The plots show that the SAR values are generally higher than the corresponding SSM/I values, sometimes by greater than 30%. This is despite adjustments already made for the reference temperature of ice (i.e., slope and offset of the line AD) to match changes in emissivities during the different phases of the summer. In some regions the SSM/I values are actually higher than 100% because of enhanced emissivities caused by moist surfaces.

The areas of large discrepancies usually occur in areas where above-freezing temperatures have been persistent. Examples of such areas are near the marginal ice zone in June and further into the interior areas in July and August. The gradients in ice concentrations near the ice edge are also consistently higher with the SAR than with the SSM/I results. The lower gradients in the SSM/I data are expected to be partly due to melt effects and partly due to the smearing of the brightness temperatures caused by the antenna side lobes and the large footprint of the SSM/I sensor.

Plots of NMC surface temperatures along the same transects are also shown. NMC data are used for the daily comparisons because the daily AVHRR data have some gaps due to persistent cloud cover. These temperature plots show that surface air temperature was always above freezing at low latitudes up to about 72°N. Along the transects, there is generally a local minimum at around 75°N and warmer temperatures at the higher latitudes. However, it is not known how accurate the data are, especially at these latitudes. The set of AVHRR images in Plate 1 is sometimes consistent with this phenomenon along the transects but generally shows slightly different distribution and colder temperatures near the north pole. The set of AVHRR images also indicates that the warmest average temperature in the Arctic occurred sometime between the last week of June and the second week of July. This is also the time period when large differences between SAR and SSM/I ice concentrations are observed (e.g., June 29, July 4, and July 10).

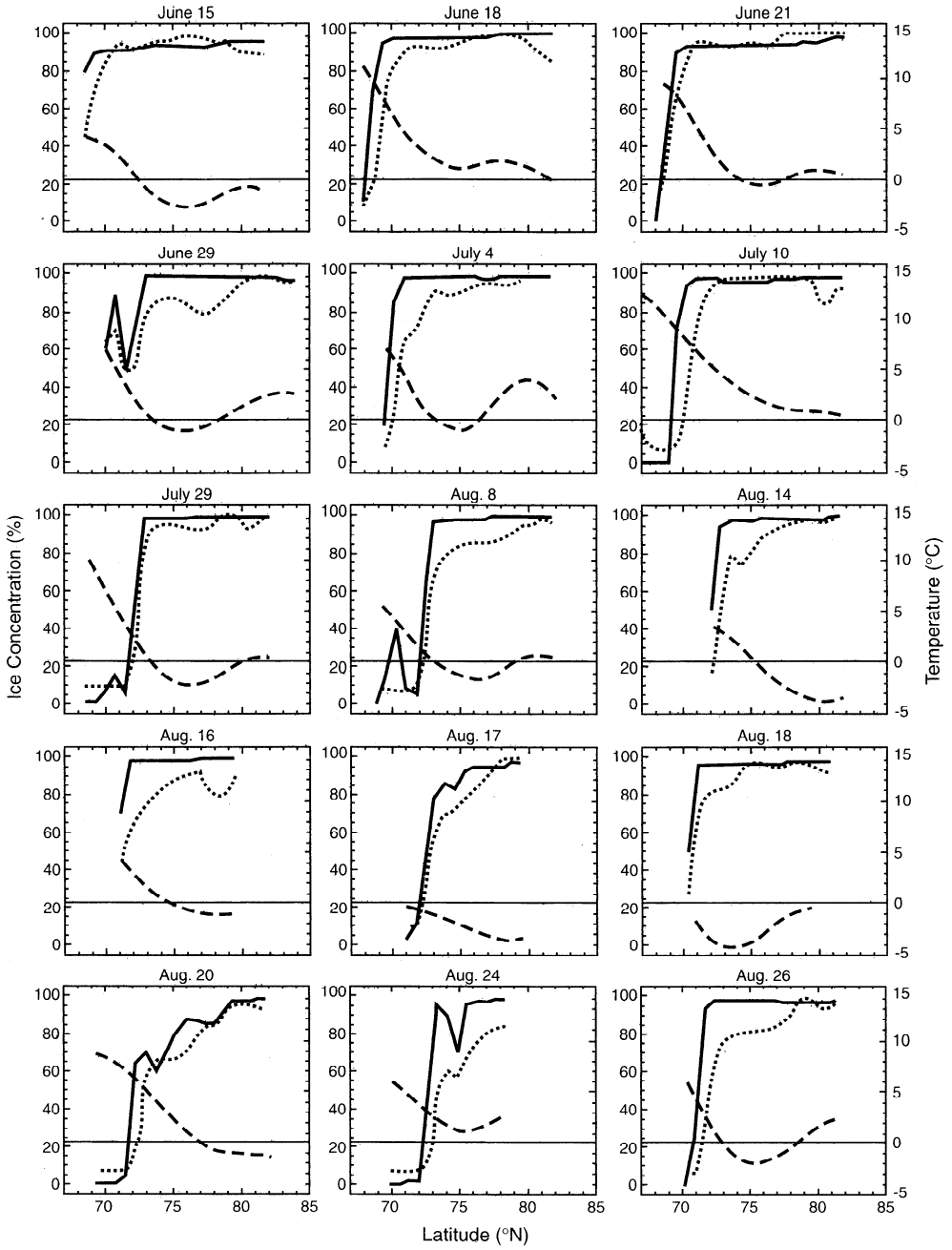

Figure 11. Plots of ice concentrations from SSM/I and SAR along transects from June 15 through August 26 and corresponding NMC surface physical temperatures.

Large differences also occurred on August 24 and 26 when the Beaufort and Chukchi Seas were experiencing relatively warm temperatures (see Plate 1).

The differences of the SAR and SSM/I values are shown quantitatively in Figure 12. The plots show the generally large differences in areas adjacent to the ice edges as indicated earlier. On June 15 the differences are largest near the marginal ice zone, while agreement is relatively good in the inner pack. On June 18 and 29 the disagreements in ice concentration start to advance further into the inner pack up to 77°N. By June 29 the disagreements were on the average about 20% up to about 78°N as the entire Arctic region warms up. During the months of July and August the location of large differences fluctuated considerably and can be substantial even at high latitudes (e.g., August 16). A plot of all the data points where comparisons were made is shown in the bottom right of Figure 12. The plot indicates that the differences are generally large at latitudes <75°N.

The ice concentrations derived from SAR show little variability with time and space, while the corresponding SSM/I ice concentrations show larger variability. The error in the SSM/I ice concentrations is expected to be large because changes in brightness temperatures are not necessarily associated with changes in ice concentration, especially in areas where melt ponding is prevalent. With SAR the supervised technique that takes advantage of the high resolution and the use of wind to identify open water make the derived values not so much dependent on the magnitude of the backscatter. While the

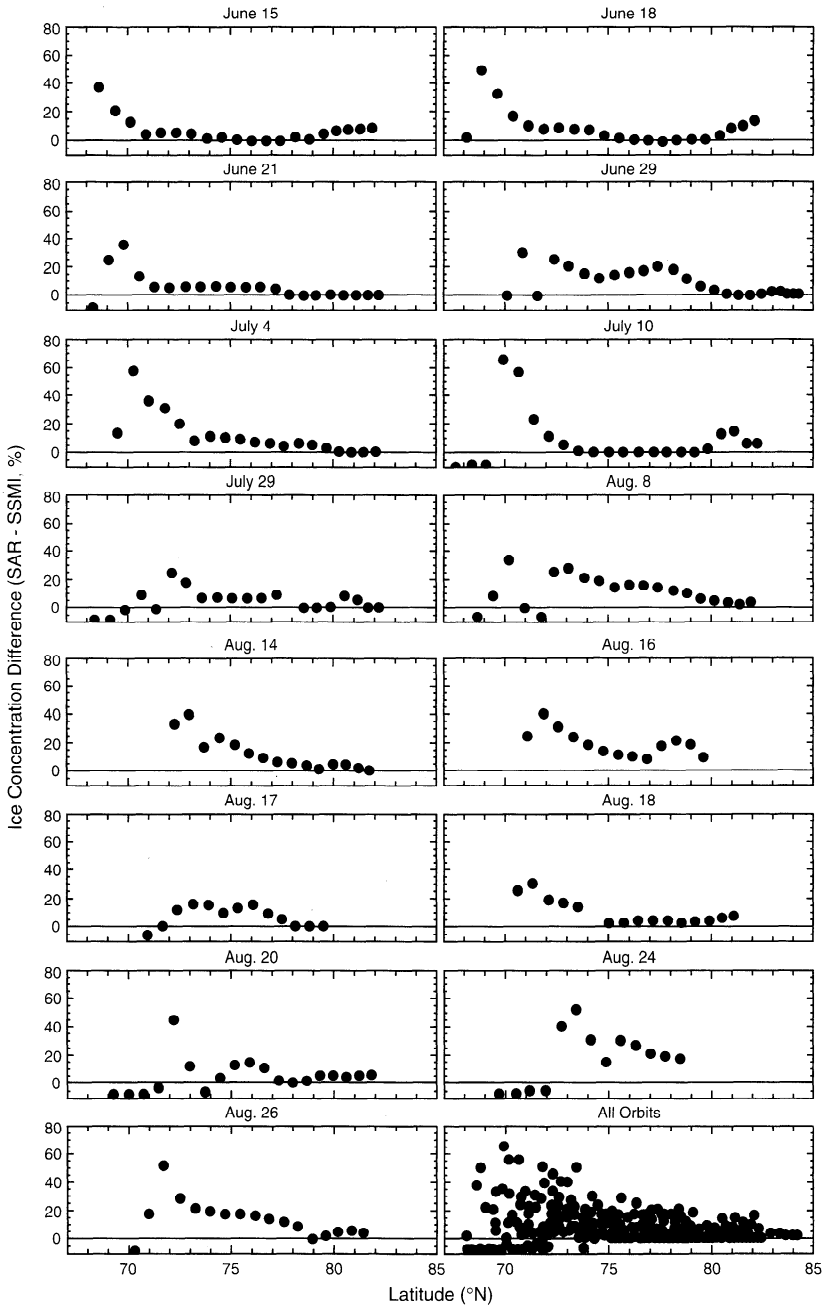

Figure 12. Plots of the differences between SAR and SSM/I ice concentrations from June 15 through August 26 and for all orbits.

absolute errors in the SAR values are not known, our analysis shows that they are likely to be small. The ice concentrations derived from SAR from winter through summer and to the subsequent winter have also been found to be consistent and coherent [*Kwok et al.*, this issue], suggesting that the SAR values may be close to the true values.

5. Albedo and Actual Summer Ice Cover

We have postulated that the primary cause of the discrepancies in the ice concentrations derived from SAR and SSM/I is the presence of melt ponds. It is important to ask whether quantitative melt-ponding information can be inferred from concurrent use of SAR and SSM/I data. Melt-ponding coverage is useful to obtain because it can be used to estimate surface albedo and to characterize the structural property of the ice material. The albedos for bare ice and melt pond have been observed to be 60% and 20%, respectively. To gain insight into the effect of melt ponds, we analyzed a high-resolution AVHRR image on July 16, 1992 (the only cloud free local area coverage (LAC) image that is available for this study), in conjunction with SSM/I data. Plate 4a shows a color-coded map of the image at 0.63 μ (channel 1) expressed in units of albedo, while Plate 4b shows the same region but at 11.0 μ (channel 4) expressed in units of temperature. The albedo increases from about 46% near the ice edge to about 54% near 75°N and drops to as low as 40% at 79°N and higher latitudes. Narrow features are visible at about 79°N and higher latitude, indicating that the ice cover was very compact in the

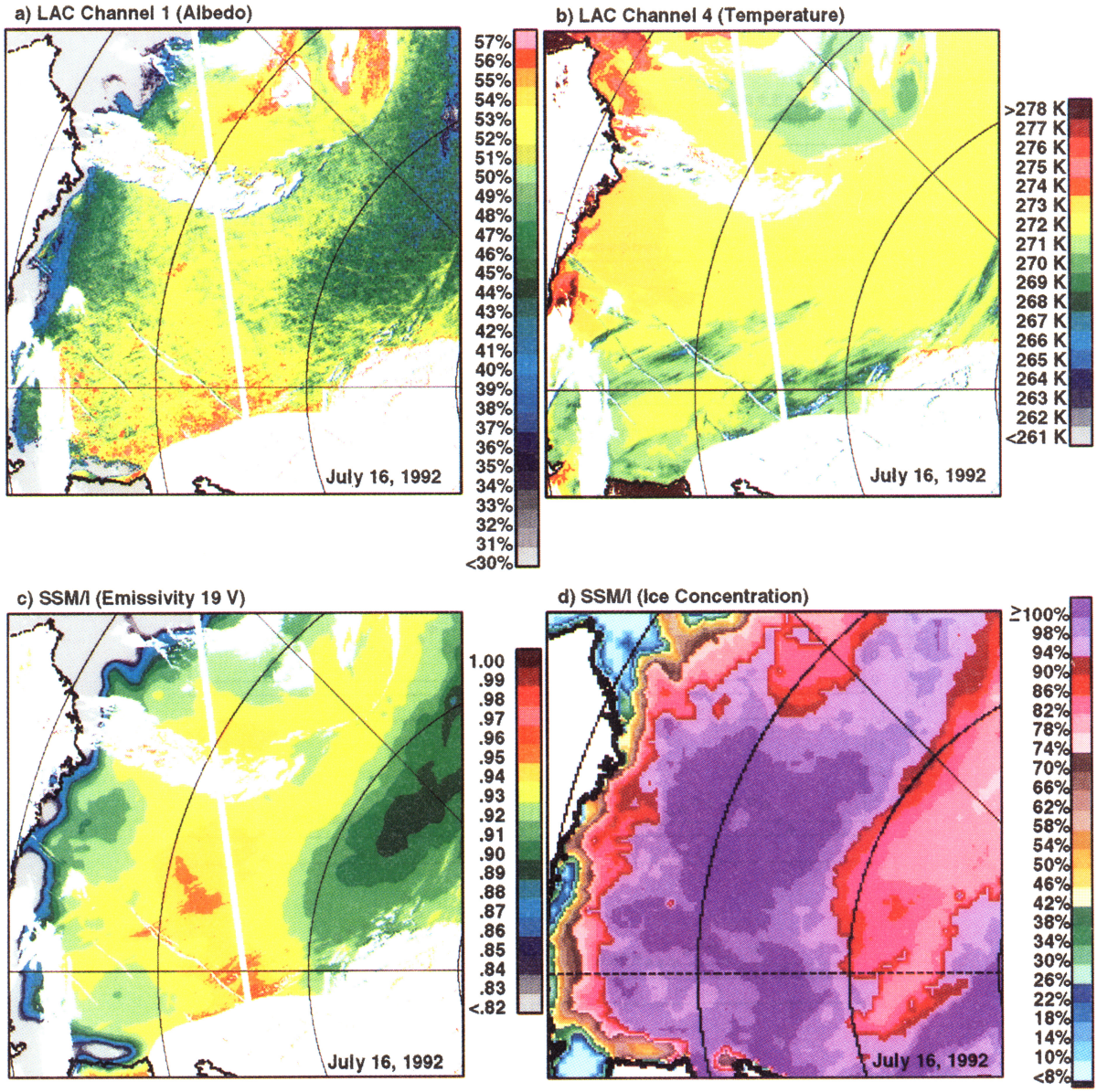

Plate 4. Surface characteristics of the Beaufort and Chukchi Sea study region on July 16, 1992: (a) albedo using high-resolution AVHRR (LAC) channel 1 data, (b) surface temperature from AVHRR (LAC) channel 4 data, (c) emissivities derived from SSM/I −19-GHz (vertical) brightness temperatures and AVHRR surface ice temperatures, and (d) ice concentrations derived from the SSM/I data.

region. A thresholding technique that classifies the visible features as open water yielded an average ice concentration of >95% at 78°N and higher latitudes. The corresponding surface emissivity map at 19 GHz (vertical polarization) derived using the ratio of SSM/I brightness temperature and ice temperature inferred from the AVHRR data is also shown in Plate 4c. In the areas where the albedo is low, the emissivity is shown to be low (suggesting melt ponding) at a time when the emissivity of ice is supposed to be high because of surface wetness. The concentration derived from the same SSM/I data, as shown in Plate 4d, was on the average 83% and as low as 74% in some areas. The temperature map indicates approximately freezing or above-freezing temperatures in most areas. If the fraction of open water at the high-latitude region was 26% as indicated by the SSM/I data, the effect of higher surface temperatures in open water areas would have been apparent. The general feature of reduced concentration at 78°N and higher latitudes was persistent for several days starting as early as on July 10 (see Plate 3), when SAR data indicate that the ice concentration was very high in the region. Melt ponds are expected to have physical temperatures close to freezing, while the open ocean may have significantly higher temperatures. The low emissivity, low albedo, and high ice concentration all strongly suggest the presence of melt ponds. However, ground truth is needed to establish that this is indeed the case.

If the true concentration C_{TR} is known, the concentration of melt ponding C_M in this region can be calculated from

$$C_M = (C_{TR} - C_{PR})/C_{TR} \tag{2}$$

where C_{PR} is the concentration derived from passive microwave radiometer (SSM/I) data. Currently, the best estimate for the true concentration may come from the SAR or Landsat. As

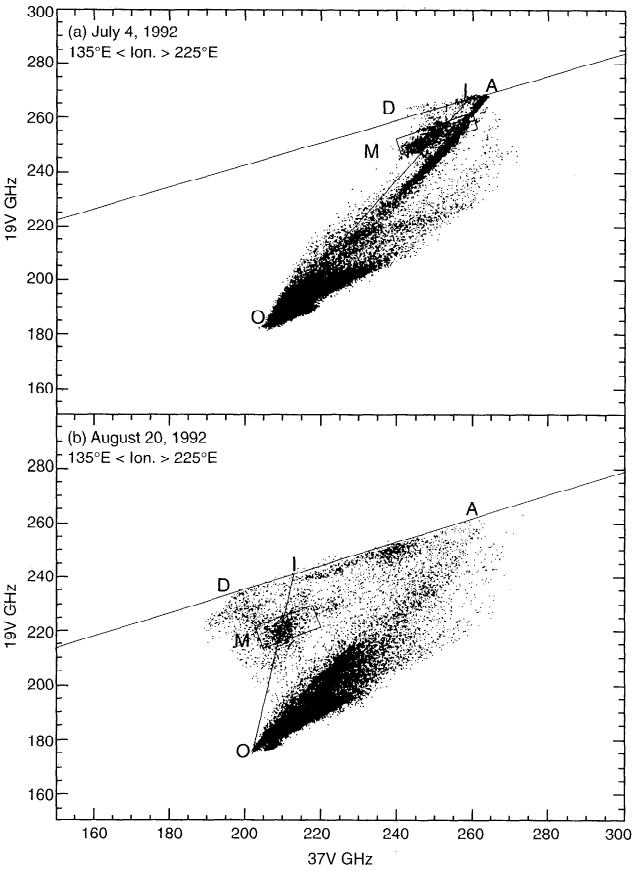

Figure 13. Scatterplots of 19-GHz versus 37-GHz brightness temperatures indicating relative location of suspected melt-ponded areas (labeled M) on (a) July 4, 1992, and (b) August 20, 1992.

an example, using the data shown in Figure 6, the average concentrations from SAR and SSM/I from 71.6°N to 77.1°N on June 23 were 97.9 and 77.2, respectively. Using (2), the melt-ponding concentration is estimated to be 21.1%. Similarly, on August 16 the average ice concentrations from 71.9°N to 79.0°N are 98.4% and 81.0% from SAR and SSM/I, respectively, yielding a melt-ponding concentration of 17.7%.

The melt-ponding concentration can also be inferred from V1937 scatter plots (e.g., Figure 4). It should be noted that the signature of melt-ponded areas during formation process is different from that during the refreezing process. In the case of the former the melt ponds are usually surrounded by surfaces that have onset of melt signatures. This is illustrated by the scatterplot in Figure 13a using data on July 4. During this time, data points with onset of melt signatures (with no melt ponding) are clustered around the point labeled A. Data from the cluster of points below A and labeled M are postulated to represent melt-ponded areas. The scatterplot for August 20 in Figure 13b illustrates the situation during freeze-up. In the plot, data points in the perennial region with multiyear ice signatures form a cluster labeled D. It is postulated as well that data points below D and labeled M are melt-ponded areas in regions where the signature of the ice cover surrounding the melt ponds is similar to those in D. Both postulates are based on high concentrations derived from SAR data in the regions represented by M. Assuming that the postulates are correct, the concentration of melt ponds can be calculated from the mixing formulation given by

$$C_M = (T_I - T_M)/(T_I - T_O) \tag{3}$$

where T_M is the brightness temperature of the melt-ponded area and T_I is the reference brightness temperature for 100% ice during summer (i.e., along AD, where A is the ice signature during the melting period and D is that during the early freeze-up period). On July 4 the centroid of the cluster identified as M would have melt-ponding ice concentration of about 20%, using (3), while on August 20, the corresponding M cluster data would have melt-ponding ice concentration of about 25%. If the clusters are well defined as in Figure 13, the precision of such determination is estimated to be better than 5%. These derived values are consistent with ship observations in the Arctic, as discussed earlier.

6. Discussion and Conclusions

Three main events that affect both the physical and radiative characteristics of sea ice during summer have been examined. The first is onset of melt (or spring/summer transition), which is easily detected because of the large change of both backscatter and emissivity of the surfaces from winter values. The signature is associated with the dielectric property of the surface when liquid water in the snow cover is present. The event does not occur simultaneously throughout the entire Arctic but generally happens in mid to late June. The second event is the formation of melt ponds caused by the removal of snow by melting, as well as the melting of the ice surface. This event causes problems in the interpretation of the data because water is opaque to microwave radiation and melt ponds over ice have the signature of open water. The third event is freeze-up, which is the condition during the summer/autumn/winter transition. During this time the surface is almost baren and dry, except for the presence of slush and snow in some areas.

A comparative analysis of coregistered SAR and SSM/I data indicates large discrepancies in the ice concentrations derived from the two sensors. In the transects studied, ice concentrations derived from SAR are shown to be consistently higher than those from SSM/I and as much as 30% in some areas. This is despite adjustments already made on the reference brightness temperature to minimize the effect of fluctuations in emissivity. Ice concentrations derived from SAR are more accurate than those from SSM/I because the much higher resolution of the former enables recognition of ice patterns within the ice pack and open water to be detected when wind effects are greater than 4 m/s. The SAR data show ice concentrations usually in the range from 90 to 98%, which is considerably higher than previous estimates from passive microwave data. AVHRR data also show higher estimates of ice concentration than passive microwave data.

It is postulated that the difference in concentrations derived from the SSM/I and SAR data is primarily due to melt ponding. The results of the analysis of the signatures and changes of these signatures over the summer period support this interpretation. If ice concentrations derived from SAR are indeed the true ice concentrations, coregistered SAR and SSM/I data can be used to estimate the percentage of melt ponding. This would be an important application since other techniques are affected by the persistent cloud cover in the Arctic during the summer. Such capability would also lead to a first-order esti-

mate of albedo which is also difficult to obtain from other techniques. Ability to apply this technique for almost the entire Arctic Region is very promising because of the advent of Radarsat data.

Acknowledgments. We are grateful to Glen Cunningham of JPL, Rico Allegrino of Hughes STX, and Larry Stock of Caelum Inc. for help in the processing and analysis of SAR, SSM/I, and AVHRR data, respectively. We thank ESA for providing ERS 1 SAR data through the Alaska SAR Facility. Also, the SSM/I data were supplied by NSIDC at the University of Colorado. This work was supported by the Cryosphere Program under NASA's Earth Sciences Division.

References

Barry, R. G., J. Maslanik, K. Steffen, R. L. Weaver, V. Troisi, D. J. Cavalieri, and S. Martin, Advances in sea-ice research based on remotely-sensed passive microwave data, *Oceanography*, *6*(1), 4–12, 1993.

Beaven, S. G., and S. P. Gogineni, Effect of summer-to-fall transition on ERS-1 SAR and SSMI images of sea ice, in *Proceedings of IGARSS'95, Firenze, Italy*, vol. 1, pp. 634–637, Inst. Electr. and Electr. Eng. Geosci. and Remote Sens. Soc., Piscataway, N. J., 1995.

Carsey, F. D., Arctic sea ice distribution at end of summer (1973–1976) from satellite microwave data, *J. Geophys. Res.*, *87*(C8), 5809–5835, 1982.

Carsey, F., Summer Arctic sea ice character from satellite microwave data, *J. Geophys. Res.*, *90*(C3), 5015–5034, 1985.

Cavalieri, D. J., B. A. Burns, and R. Onstott, Investigation of the effects of summer melt on the calculation of sea ice concentration using active and passive microwave data, *J. Geophys. Res.*, *95*(C4), 5359–5369, 1990.

Comiso, J. C., Sea ice microwave emissivities from satellite passive microwave and infrared observations, *J. Geophys. Res.*, *88*(C12), 7686–7704, 1983.

Comiso, J. C., Characteristics of winter sea ice from satellite multispectral microwave observations, *J. Geophys. Res.*, *91*(C1), 975–994, 1986.

Comiso, J. C., Arctic multiyear ice classification and summer ice cover using passive microwave satellite data, *J. Geophys. Res.*, *95*(C8), 13,411–13,422, 13,593–13,597, 1990.

Comiso, J. C., Surface temperatures in the polar regions using Nimbus 7 temperature humidity infrared radiometer, *J. Geophys. Res.*, *99*(C3), 5181–5200, 1994.

Comiso, J. C., SSMI sea ice concentrations using the bootstrap algorithm, *NASA Ref. Publ., RP 1380*, 49 pp., 1995.

Comiso, J. C., T. C. Grenfell, M. Lange, A. Lohanick, R. Moore, and P. Wadhams, Microwave remote sensing of the Southern Ocean ice cover, in *Microwave Remote Sensing of Sea Ice*, *Geophys. Monogr. Ser.*, vol. 68, edited by F. Carsey, chap. 12, pp. 243–259, AGU, Washington, D. C., 1992.

Donelan, M. A., and W. J. Pierson Jr., Radar scattering and equilibrium ranges in wind-generated waves with application to scatterometry, *J. Geophys. Res.*, *92*(C5), 4971–5029, 1987.

Eicken, H., M. Lensu, M. Lepparanta, W. B. Tucker III, A. J. Gow, and O. Salmela, Thickness, structure, and properties of level summer multiyear ice in the Eurasian sector of the Arctic Ocean, *J. Geophys. Res.*, *100*(C11), 22,697–22,710, 1995.

Emery, W. J., C. Fowler, and J. Maslanik, Arctic sea ice concentrations from special sensor microwave imager and advanced very high resolution radiometer satellite data, *J. Geophys. Res.*, *99*(C9), 18,329–18,342, 1994.

Eppler, D., et al., Passive microwave signatures of sea ice, in *Microwave Remote Sensing of Sea Ice*, *Geophys. Monogr. Ser.*, vol. 68, edited by F. Carsey, chap. 4, pp. 47–71, AGU, Washington, D. C., 1992.

Gloersen, P., W. Campbell, D. Cavalieri, J. Comiso, C. Parkinson, and H. J. Zwally, Arctic and Antarctic sea ice, 1978–1987: Satellite passive microwave observations and analysis, *NASA Spec. Publ. 511*, 1992.

Grenfell, T. C., Surface-based passive microwave studies of multiyear ice, *J. Geophys. Res.*, *97*(C3), 3485–3501, 1992.

Grenfell, T. C., and A. Lohanick, Temporal variations of the microwave signatures of sea ice during the late spring and early summer near Mould Bay NWT, *J. Geophys. Res.*, *90*(C3), 5063–5074, 1985.

Gogineni, S. P., R. K. Moore, T. C. Grenfell, D. G. Barber, S. Digby, and M. Drinkwater, The effects of freeze-up and melt processes on microwave signatures, in *Microwave Remote Sensing of Sea Ice*, *Geophys. Monogr. Ser.*, vol. 68, edited by F. Carsey, chap. 17, pp. 329–341, AGU, Washington, D. C., 1992.

Key, J., and M. Haefliger, Arctic ice surface temperature retrieval from AVHRR thermal channels, *J. Geophys. Res.*, *97*(D5), 5885–5893, 1992.

Kwok, R., and G. F. Cunningham, Backscatter characteristics of the winter ice cover in the Beaufort Sea, *J. Geophys. Res.*, *99*(C4), 7787–7802, 1994.

Kwok, R., E. Rignot, B. Holt, and R. G. Onstott, Identification of sea ice types in spaceborne SAR data, *J. Geophys. Res.*, *97*(C2), 2391–2402, 1992.

Kwok, R., J. C. Comiso, and G. Cunningham, Seasonal characteristics of the perennial ice cover of the Beaufort Sea, *J. Geophys. Res.*, this issue.

Manabe, S., and R. J. Stouffer, Multiple-century response of a coupled ocean-atmosphere model to an increase of atmospheric carbon dioxide, *J. Clim.*, *7*(1), 5–23, 1994.

Massom, R., and J. C. Comiso, The classification of Arctic sea ice types and the determination of surface temperature using advanced very high resolution radiometer data, *J. Geophys. Res.*, *99*(C3), 5201–5218, 1994.

McClain, E. P., W. Pichel, and C. Walton, Comparative performance of AVHRR based multichannel sea surface temperatures, *J. Geophys. Res.*, *90*(C6), 11,587–11,601, 1985.

Onstott, R. G., SAR and scatterometer signatures of sea ice, in *Microwave Remote Sensing of Sea Ice*, *Geophys. Monogr. Ser.*, vol. 68, edited by F. Carsey, chap. 5, pp. 73–104, AGU, Washington, D. C., 1992.

Onstott, R., T. C. Grenfell, C. Matzler, C. A. Luther, and E. A. Svendsen, Evolution of microwave sea ice signatures during early summer and midsummer in the marginal ice zone, *J. Geophys. Res.*, *92*(C7), 6825–6835, 1987.

Parkinson, C. L., J. C. Comiso, H. J. Zwally, D. J. Cavalieri, P. Gloersen, and W. J. Campbell, Arctic sea ice 1973–1976 from satellite passive microwave observations, *NASA Spec. Publ. 489*, 1987.

Thomas, D. R., and D. A. Rothrock, The Arctic ocean ice balance: A Kalman smoother estimate, *J. Geophys. Res.*, *98*(C6), 10,053–10,067, 1993.

Weeks, W. F., and S. F. Ackley, The growth, structure, and properties of sea ice, in *Geophysics of Sea Ice*, *NATO ASI Ser., Ser. B*, vol. 146, edited by N. Untersteiner, pp. 9–164, Martinus Nijhoff, Dordrecht, Netherlands, 1986.

Winebrenner, D. P., E. D. Nelson, and R. Colony, Observations of melt onset on multiyear Arctic sea ice using the ERS 1 syntetic aperture radar, *J. Geophys. Res.*, *99*(C11), 22,425–22,441, 1994.

Yamanouchi, T., and K. Seko, *Antarctica from NOAA Satellites—Clouds, Ice, and Snow*, 91 pp., Natl. Inst. of Polar Res., Tokyo, Japan, 1992.

Zwally, H. J., and P. Gloersen, Passive microwave images of the polar regions and research applications, *Polar Rec.*, *18*, 431–450, 1977.

J. C. Comiso, Laboratory for Hydrospheric Processes, NASA Goddard Space Flight Center, MC 971, Greenbelt, MD 20771. (e-mail: comiso@joey.gsfc.nasa.gov)

R. Kwok, Jet Propulsion Laboratory, California Institute of Technology, Mail Stop 300-235, 4800 Oak Grove Drive, Pasadena, CA 91109.

(Received December 1, 1995; revised August 22, 1996; accepted August 28, 1996.)